Lab Scale Modelling of Collision Generated Spray in the Context of Marine Icing

A thesis submitted to the School of Graduate Studies
in partial fulfilment of the requirements for the degree of
Master of Engineering

Faculty of Engineering & Applied Science
Memorial University of Newfoundland

October 2016

St. John's Newfoundland

Abstract

Marine icing is a form of ice accretion that affects vessels in harsh environmental conditions. This type of ice accretion is primarily due to collision generated spray icing. Consequences of marine icing range in severity from capsizing of small fishing vessels to hazardous working conditions and reduced operational efficiency in larger vessels and rigs. The understanding of icing effects are mainly limited to atmospheric icing in the aircraft industry, while there is a limited amount of new literature and industrial knowledge regarding marine spray icing. The objective of this project was to understand the characteristics of collision generated spray at the lab scale. In this effort, experiments were conducted with three fabricated models of varying geometries in a tow tank that were subjected to oncoming waves. Wave probes measured the wave characteristics while pressure sensors and a high speed camera recorded impact pressure and spray generation imaging, respectively. The impact pressure and imaging data files largely serve as validation data for follow on research. Trends were observed and plotted that correlate increasing impact pressures with increasing wave steepness values. A qualitative summary of the spray characteristics captured through imaging found that higher instances of notable spray events occurred as wave impact pressure increased.

Acknowledgements

Acknowledgements are due to several key people who have assisted and aided in the completion of this thesis. First, the advisement from Dr. Yuri Muzychka and Dr. Greg Naterer is greatly appreciated. Learning from their combined experience and research expertise has been a great opportunity. Learning from the past experiences and recommendations of the other professors in the Marine Icing research group has also been rewarding. The discussions and brainstorming with all of the student members of the group have been particularly fruitful, however, the insights gained from working with Armin Bodaghkhani should be noted.

Much of the work undertaken in the lab could not be accomplished without the assistance of the laboratory technicians Trevor Clark, Matt Curtis, and Craig Mitchel. Thanks are also due to the Technical Services personnel of David Snook and Billy Bidgood.

Finally, the completion of this program would not have been accomplished without the funding support from Dr. Muzycka and Dr. Naterer, in addition to Statoil and Mitacs contributions.

Contents

Nomenclature

α	Model angle with respect to vertical plane
β	Model side panel angle
β_o	Collision efficiency at cylinder stagnation point
Δt_{ds}	Time duration of impinging spray
$\frac{dC(r_{80})}{dr_{80}}$	Spray concentration function
$\frac{dH_i}{dt}$	Rate of ice formation
$\frac{dL}{dt}$	Icing rate
γ	Angle between spray and ship velocity vectors
ν	air dynamic viscosity
τs	time of the spray flight of the droplets to impact (reword)
φ	Langmuir's parameter
ζ	Collection efficiency
a	Droplet radius
C_d	droplet drag coefficient
C_w	Specific heat of water
D	Droplet diameter
E_c	Collection efficiency

E_M	Total collision efficiency
F	Fraction of water left after initial freezing occurs
H	Wave height
h'	Elevation above ship deck
$H_{1/3}^2$	Significant wave height
H_s	Wave height, root mean square
K	Stokes number
k	Wave steepness
L_f	Latent heat of freezing for saline water
L_w	Wavelength
LWC	Liquid Water Content
m	Total spray flux
m'	Time averaged spray flux density
$MSFV$	Medium Sized Fishing Vessel
P	Impact pressure
R_i	Rate of ice growth per unit area
R_w	Local water catch rate
Re	Reynolds Number
T_a	Temperatures of air
T_f	Temperatures of saline water at its freezing point

T_w	Temperatures of sea water
T_w	Wave period
U	Spray speed
U_{10}	Wind speed $\geq$ 15 m/s
U_{rs}	Relative spray speed
V	Ship speed
V_a	Wind Speed
V_r	Ship speed relative to wave
w	Liquid water content, time averaged
z	Vertical height above sea level (m)

List of Tables

List of Figures

Chapter 1

Introduction

1.1 Introduction

Ice accretion is an environmental hazard that affects maritime shipping and offshore structures that operate in harsh conditions, primarily in northern, Arctic regions. Marine icing is the build up of ice on ocean going vessels or stationary structures in these high latitudes, and can be comprised of a combination of saline sea icing and fresh water atmospheric icing. Atmospheric icing is caused when fog, rain, snow, or other atmospheric moisture freezes onto a surface. This type of icing has been researched more in depth compared to marine icing largely due to its relevance in the aerospace industry. The icing effects due to sea spray are caused by two mechanisms: wind generated spray, and collision generated spray. A more detailed discussion of these mechanisms will be continued in Chapter 2. The dominant factor causing wind generated spray is high wind velocities that shear off the top off wave crests, although spray can be generated by bubbles bursting or white-caps (Wu, 1979). Collision generated spray occurs when a wave collides with a vessel or stationary structure, which causes subsequent spray droplets to be formed, and is the dominant mechanism in marine icing (Zakrzewski, 1987). The sum total of the contribution of water content from atmospheric sources, and both wind and wave generated sea spray is ultimately

(a) Vessel Icing (Timco and Kubat, 2005)

(b) Structure Icing (Minsk, 1984)

Figure 1.1: Depictions of Vessel and Structure Icing

what creates the final observable ice accretion. The effects of marine icing have wide ranging levels of severity (Ryerson, 2013). Some of the more minor effects of icing occur when ship doors, surfaces, ventilation faces, and outer features are iced over. The consequences of this icing include slipping and tripping hazards to workers and overall operational disruption, especially if ship or structure parts are iced shut. The more severe effects of marine ice accretion can be catastrophic. The centre of gravity of a smaller fishing vessel can be affected to the extent from ice build up that capsizing occurs. Further research into understanding and predicting marine icing is also motivated by industry moving operations further into higher latitudes and Arctic waters.

The severity of ice accretion on ships has been known for over a century (Nature, 1881), however, early modern reports of marine icing did not appear until the 1950's (Sutherby, 1951; Hay, 1956). These early reports, among others, necessitated the extensive collection of field data beginning in the 1960s and 1970s (Itagaki, 1977;

Kachurin et al., 1974). The early marine icing researchers collected field data of marine ice accretion aboard medium sized fishing vessels (MSFV) in Japanese and Soviet fishing waters. The most recent collection of icing data in a field environment was conducted in the early 1990s, and was motivated by the need for icing data for a vessel different than a fishing vessel. In this case, the vessel class studied was a US Coast Guard cutter (Ryerson, 1995).

The early modelling and forecasting of marine icing was empirically based from extensive field observations, and nomograms were then subsequently generated that acted as a visual prediction tool. Two examples of these purely observational prediction tools are below in Figures 1.2 and 1.3 (Sawada, 1962; Mertins, 1968). Twelve years

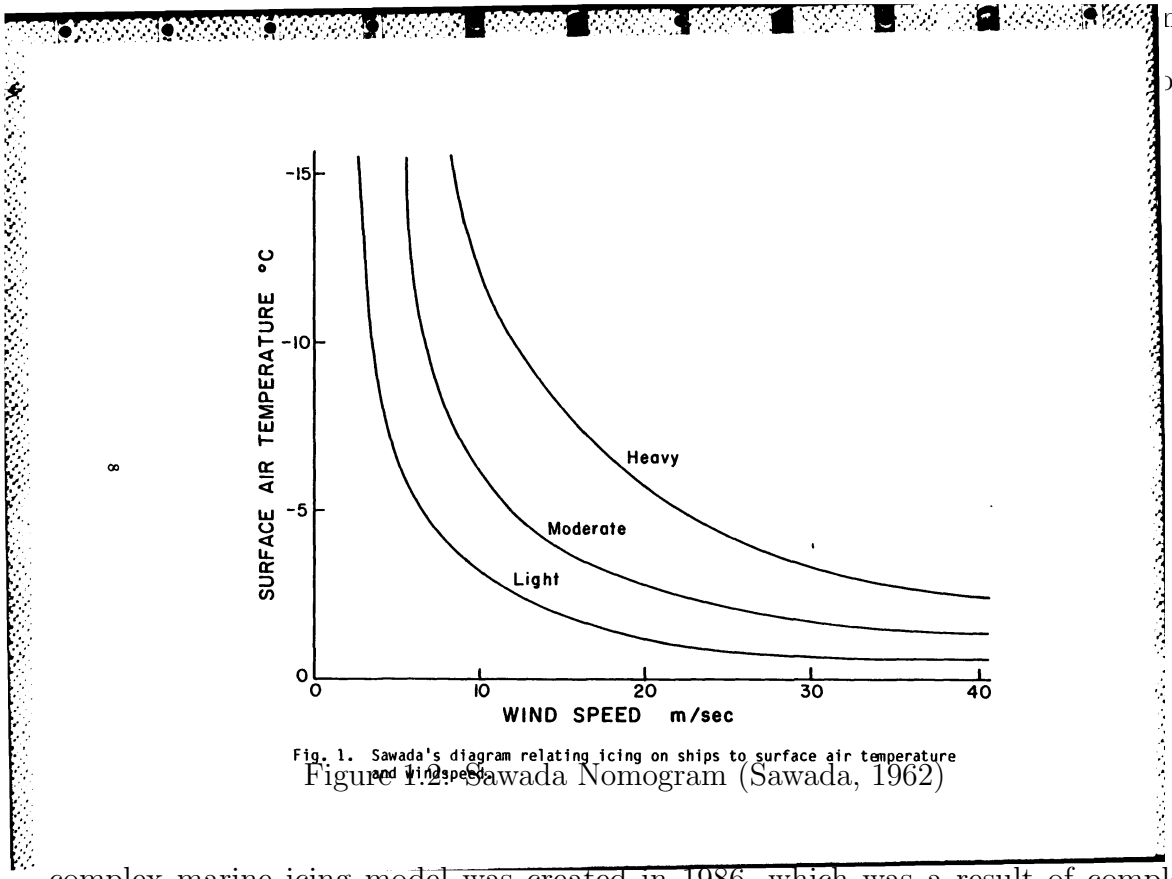

Figure 1.2: Sawada Nomogram (Sawada, 1962)

complex marine icing model was created in 1986, which was a result of complex statistical analyses of 195 icing incidents, of which 58 were deemed valid for reliable

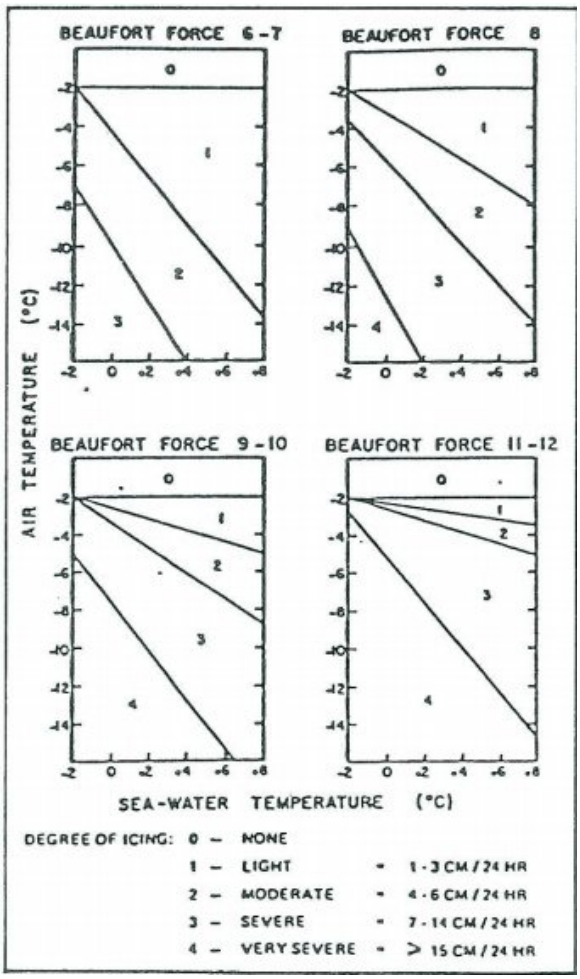

Figure 1.3: Mertins Nomogram (Mertins, 1968)

analysis (Overland et al., 1986). The categorical icing algorithm developed by Overland et al. (1986) is valid for vessels ranging from 20-75 m in length, and is a function of meteorological conditions. The sensible heat flux was identified as the main influence of icing, and an icing predictor in the algorithm was simplified from the heat balance (Overland et al., 1986):

$$\frac{dH_i}{dt} \propto \frac{V_a(T_f - T_a)}{1 + \Phi(T_w - T_f)} \tag{1.1}$$

Where $\frac{dH_i}{dt}$ is the rate of ice formation, V_a is the wind speed, T_f, T_a, T_w, are the temperatures of saline ice at its freezing point, air, and sea water, respectively. Also,

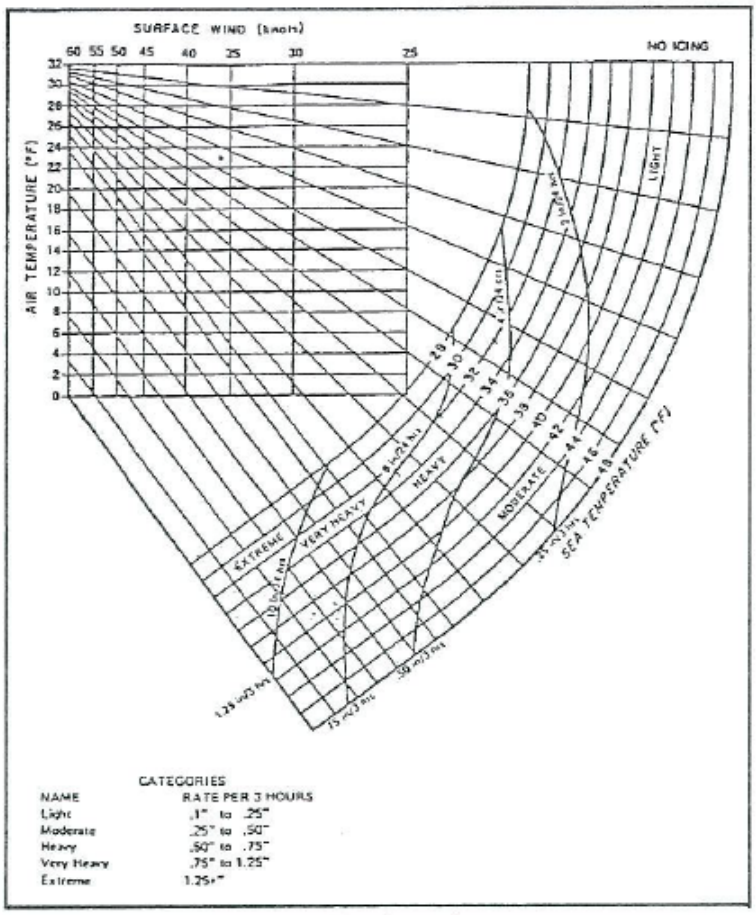

Figure 1.4: Wise and Cominksy Nomogram (Wise and Cominksy, 1980)

$\Phi = C_w/L_f F$ where C_w is the specific heat of water, L_f latent heat of freezing for saline water, and F is the fraction of water left after initial freezing occurs. The physical meaning of Φ is the first order dependence of ice accretion on seawater temperature and was empirically determined to be 0.4 $^\circ C^{-1}$. Finally, the algorithm's icing prediction equation becomes:

$$PR = \frac{V_a(T_f - T_a)}{1 + 0.4(T_w - T_f)} \tag{1.2}$$

It is interesting to also note that the meteorological forecasting of marine icing

published by NOAA still uses the same algorithms developed in the 1980s (NOAA, 2016). An example graphic that is made available online in real time can be seen in Figure 1.5. Analytical modelling of marine icing started to emerge in the 1970s and

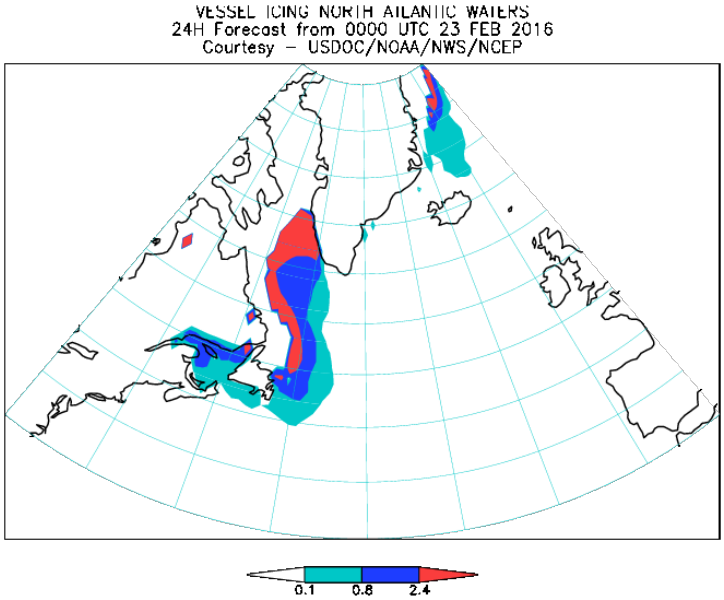

Figure 1.5: NOAA Icing Prediction (NOAA, 2016)

1980s, and used the previous field data collected as input parameters. Knowledge of the heat transfer and thermodynamic processes of saline droplet freezing is needed for the development of the icing models. Understanding spray behaviours is also required, which includes knowing droplet velocities and quantities of liquid water content (LWC) that impinge and freeze onto surfaces. Modelling of the ice accretion on a ship was simplified by using the assumption that the ship structure could be broken down into simple circular cylinders and flat plates, which act as the surfaces upon which droplet impingement occurs. Laboratory scale experimental works were also conducted in investigating the droplet collection efficiency, heat transfer, and icing on circular cylinders, among other things. Further discussion of these topics will

be continued in Chapter 2.

1.2 Thesis Research Motivations

The research conducted for this Masters thesis was in conjunction with the Marine Icing research group at Memorial University, which had eight student participants. The group was comprised of five masters students and three PhD candidates, whose fields were mechanical engineering, electrical engineering, and applied mathematics. The group was funded in part by Statoil, a Norwegian oil and gas company, under a Mitacs program. Part of the program included collaboration and communication with Statoil, and understanding the role of marine icing in their research plans. Student research aims and focusses were subsequently broken up in a strategic manner, covering the fields of experimental, analytical, and numerical research.

The field of research for this thesis centred around experimental laboratory research, focussing on the spray generated upon wave impact of a vessel, also known as collision generated spray. The goal was to develop and build laboratory scale models and test methods to measure the characteristics of lab scale spray generation, which ultimately contribute to the marine icing process. Historically, experimental studies have been done at full scale, being extensive not only in time, but monetarily as well (Roebber and Mitten, 1987). The motivation for this laboratory scale modelling lies in the relatively small amount of laboratory tests in this field, and in the need for validation data. The challenges and complexities of laboratory scale modelling of the spray formation of vessels was illustrated by Lebiednzinksi and Thomas (1993), but also noted that scale modelling could still be useful in understanding other parameters, such

as droplet velocities. A previous study that measured the collision generated spray flux on a scale model of a fishing vessel obtained favourable results, and developed predictive empirical relations (Chung et al., 1998). That study only measured the geometric distribution and overall quantity of the spray flux, but did not measure other parameters such as spray velocity, or the size and quantity of the droplets. This thesis attempts to expand upon this by testing the wave impacts upon models of varying geometries and investigating the behaviours of the initial vertical sprays that are developed. Furthermore, the results are intended to provide experimental data as validation for other group members' research.

1.3 Preface to Following Chapters

The following chapters in this thesis are broken down systematically into a step by step manner. The purpose of this current chapter was to introduce and discuss the context of this thesis was well as provide some background research motivations. Chapter Two contains a review of the literature pertaining to marine icing, the subject that forms the basis and foundation for this thesis. The aim is to first provide a background synopsis and historical review of the field of marine icing so that the subject can be fully appreciated in context. What follows is a review of several important experimental works concerning marine icing. The overall process of marine icing is then discussed from each step in the process. The purpose of this is to provide enough background to fully appreciate the importance of collision generated spray in the marine icing process. Chapter Three contains the experimental objectives, an overview of test facilities used, uncertainty estimates, and the experimental methodology. The results of the experimental results are then summarized in Chapter Four, and finally, conclusions

and recommendations are outlined in Chapter Five.

Chapter 2

Literature Review

The following literature review follows and outlines the components that contribute to marine icing in a logical, step by step manner. This chapter is composed of several different sections. First, a brief overview of past marine icing works is given to provide historical perspectives and context to the current state of marine icing research. Influential laboratory experimental work is then summarized for a handful of studies that are frequently cited and used in subsequent modelling of icing. Next, the theory behind the individual processes of marine icing is described, after having an understanding of its historical context. The individual components of marine icing that are described below are spray generation, spray droplet trajectory, droplet impingement and solidification phase change upon impact. There are several gaps in the literature that should be noted. The most relevant is the lack in modern research in sea spray formation for vessel types, from a modelling standpoint. Even more so, there is a lack in laboratory scale studies into spray formation. These gaps will be focused upon below in discussions of this thesis.

2.1 Historical Background

Awareness of marine icing has existed for over a century, as maritime operations and industrial ventures have moved farther into harsh northern climates (Nature, 1881). Some of the earliest reporting to icing of ships was a result of the icing of British naval ships operating in northern waters during World War I and World War II (Sutherby, 1951). The report by Sutherby (1951) concluded that marine icing was largely a function of wind speed, sea water temperature (-1.7° – 0°C), and air temperature (-15° – -6.7°C). He finalized the report by describing the de-icing technique of the time as using ice picks, and discussed the future of anti-icing materials that we now know as hydrophobic coatings. The fatal losses of British fishing trawlers Lorella and Roderigo in 1955 necessitated an official inquiry into their causes, which was completed by Hay (1956). He concluded that a combination of atmospheric and sea spray icing contributed to the two trawlers' sinking, with sea spray icing being the dominant mechanism. He provided calculations for the icing rates, but were rough approximations at best. The spray quantity was an assumed quantity (50 kg/wave) and the collision efficiency was assumed to be unity, which we now know is not exactly correct in all cases.

While the knowledge of icing has existed for some time, it was not until the 1960s and 1970s that field measurements of marine icing on ships began to be published. Field data at that time primarily came from two main sources, namely, Japanese and Soviet researchers (Itagaki, 1977; Kachurin et al., 1974). These early field studies measured both marine icing rates for ships in Japanse waters (Tabata et al., 1963), as well as meteorological conditions contributing to icing and spray fluxes (Tabata, 1969). The initial icing rates were determined by using a vertical metal rod to act as an ice

collection point, from which the added ice mass could be measured. Beneath that was an icing gage that served to measure the run-off brine, accounting for total impacting mass (Tabata et al., 1963). The correlations developed between weather conditions and icing events were driven by ship operators' feedback to the researchers. Tabata's inital spray flux measurement devices were rudimentary water absorbing circular cylinders, which were placed across the ship. The added water mass from spray events could then subsequently measured. This technique of directly measuring spray flux by measuring water mass in water collectors was eventually used in a similar manner that was used in the development of the RIGICE model (Muzik and Kirby, 1992). This model will be explained further in the literature review. Lab scale modelling of the spray flux in the 1990s also utilized the cylindrical collector approach (Chung et al., 1998).

Several of the early Soviet researchers in marine icing during the 1960s and 1970s include Panov, Kachurin, and Borisenkov, among others (Zakrzewski and Lozowski, 1988; Lozowski et al., 2000). Their approaches were somewhat similar to the Japanese researchers in the sense that they used field data to make their correlations used in predicting icing.

Research in the 1980s through to the present has still included field data measurements (Ryerson, 1995) but has also introduced some laboratory scale experiments investigating heat transfer characteristics of icing (Achenbach, 1977; Lozowski et al., 1983b; Makkonen, 1985). Several models began to emerge for both vessel and structure icing, with the structure icing models named RIGICE and ICEMOD and motivated by the oil and gas industry's expanding operations (Stallabrass, 1980; Roebber and Mitten, 1987; Brown and Horjen, 1989). Laboratory scale experiments investigating spray flux also served as a basis for a numerical icing model of a fishing vessel (Chung

et al., 1998; Chung and Lozowski, 1998).

2.2 Influential Laboratory Experiments Pertaining to Marine Icing

Marine icing studies and models are largely based off of field data sets of sea spray, meteorological conditions, and vessel configurations that lead to ice formation. These data sets originated mostly from Soviet and Japanese researchers in the 1960s and 1970s. There are a handful of laboratory scale experiments that have been influential in the study of marine icing at a fundamental level, which have in turn served as aids in the development of prediction and modelling methods. These experiments mostly contributed to the greater understanding of the heat transfer and solidification processes of impacting spray.

One of the first studies that is highly cited was conducted by Achenbach (1977). The reason this study was so applicable and relevant to marine icing modelling lies in the fact that as ice accretion occurs, the iced surfaces inherently change shape and become more irregular. As the the iced surface becomes rougher and more turbulent, the heat transfer increases. A two-part series published in the early 1980s has also been influential to the ongoing study of marine icing. An initial analytical model for icing of a smooth circular cylinder was developed by Lozowski et al. (1983a). The follow up study by Lozowski et al. (1983b) conducted icing experiments on a circular cylinder with fresh water and compared the physical results to the previous prediction model, finding favourable results. Later, Makkonen (1985) developed an improved model for the heat transfer of a rough, iced circular cylinder for a range of

$5 \times 10^4 \leq Re \leq 4 \times 10^6$. Comparison to the experimental data collected by Achenbach (1977) showed favourable agreement. Another study that compared experimental results to theoretical prediction was Makkonen and Stallabrass (1987). Spray cloud collision efficiencies on a circular cylinder were compared to the theoretical predictions of Finstad and Lozowski (1988), and good agreement was also found. It was noted in this study that the collision efficiency formulation of Langmuir and Blodgett (1946) was improved upon by Finstad and Lozowski (1988), which should be used in future calculations.

An interesting laboratory scale experiment studying the incoming spray flux was conducted at the National Research Council, Canada, in St. John's, Newfoundland in the late 1990s (Chung et al., 1998). What stands out is that it is the only experiment found in the literature that studied the spray distribution of a fishing trawler in a laboratory setting, as opposed to taking field measurements. The spray flux was measured with a series of cylindrical water catch devices, similar to what has been used on full scale vessels. The outcome from Chung et al. (1998) was the formulation of empirical equations modelling the spray distribution of the particular vessel. These relations were subsequently incorporated into a simulation model of ice accretion of the same vessel, whose results had physically realistic results (Chung and Lozowski, 1998).

Finally, although not conducted in a lab setting, it is worth mentioning the study conducted by Ryerson (1995). This study measured the spray flux and ice accretion of the US Coast Guard Cutter *Midgett*, which is larger than the fishing trawlers in previous studies. Ryerson (1995) found that for this particular vessel's cruise, the spray droplet size range was 14 to 7700 μm and their median size was 234 μm. Calculating the median droplet size provides a way to somewhat simplify the calculation of the

collision efficiencies (Finstad et al., 1988). They also found that the concentration of the incoming spray clouds ranged from 2.0×10^5 to 3.0×10^5 drops m^{-3}. After having a brief background summary of marine icing and some of the influential experimental works, the next sections will discuss the components of marine icing. The aim is to bring the topic of this thesis, spray generation in the context of marine icing, into the context of the larger picture of the icing process.

2.3 Spray Generation

The generation of spray that is attributable to marine icing can be separated into two categories: wind generated spray and collision generated spray. A third source that can contribute to overall marine icing is not saline, as in sea spray, but fresh water atmospheric moisture. The following two sections discuss the understanding of the two types of sea spray generation that can contribute to marine icing.

2.3.1 Wind Generated Spray

There are several ways that wind generated spray occurs, with the wind blowing the tops off of waves in whitecaps and air bubbles bursting being the dominant causes (Wu, 1979). While wind generated sea spray does not significantly contribute to vessel icing as opposed to collision generated spray, it does, however, play an important role in the icing of marine superstructures such as offshore oil platforms. As such, it should still be noted here in its role in the overall subject of marine icing.

Horjen and Vefsnmo (1984) based a formulation for wind generated sea spray off of empirically derived data sets, which was later improved by Roebber and Mitten (1987) and is given as:

$$w = w_o\left(\frac{U_{10}}{U_{REF}}\right)^{3.4}\exp\left(\frac{H}{2} - z\right) \tag{2.1}$$

where w = liquid water content (kg m^{-3}), w_o = 9.45 x 10^{-6} kg m^{-3}, U_{10}= wind speed $\geq$ 15 m/s, U_{REF}= 15 m/s, H = wave height in meters, and z = elevation above mean sea level $\geq H/2$. It should be noted again that since this formulation was the result of the improvement by Roebber and Mitten (1987) in the context of the MARICE icing model, it is relevant for wind spray against superstructures. A more recent model for wind generated sea spray was created by Jones and Andreas (2011), where a number of previous works of spray generation and concentration functions are compared. Jones and Andreas (2011) then concluded with their own, improved, formulations of wind generated spray concentration functions, concentration profile, and liquid water content of the spray. The spray concentration function for larger drops (radius geometric mean between 0.1 - 25μm) is given by:

$$\frac{dC(r_{80})}{dr_{80}}[m^{-3}\mu m^{-1}] = \frac{7\times 10^4 U_{10}^2}{r_{80}}\exp\left(-0.5\left[\frac{\ln(r_{80}/0.3)}{\ln 2.8}\right]^2\right) \tag{2.2}$$

where $r_{80} = 0.3$ μm and wind velocity U_{10} is ranges between 5 and 20 m s^{-1}. Jones and Andreas (2011) then give the following equation for a spray concentration that includes the generation of spume droplets, which becomes more evident at wind speed in excess of roughly 20 m s^{-1}:

$$\frac{dC(r_{80})}{dr_{80}}[m^{-3}\mu m^{-1}] = \frac{30 U_{10}^4}{r_{80}}\exp\left(-0.5\left[\frac{\ln(r_{80}/0.3)}{\ln 4}\right]^2\right) \tag{2.3}$$

It is interesting to note that these spray concentration functions can be considered one of the most recent developments in describing marine icing caused from wind spray. One example is the 2014 model that included these spray functions developed by Kulyakhtin and Tsarau (2014).

2.3.2 Collision Generated Spray

Collision generated spray, or wave generated spray, is formed when waves collide with either a vessel or stationary structure such as an offshore oil rig. Historically, almost all of the spray generation modelling equations have been based on experimental field measurements for spray flux and liquid water content. Furthermore, most of these formulations characterizing collision generated spray seem to be mostly a function of the colliding wave height, and since they are derived from field measurements, they tend to be applicable for those certain conditions only. Several commonly cited equations for the collision generated wave spray found in the literature are summarized below.

Forest et al. (2005) developed an equation for LWC as a function of height that is used in the RIGICE04 computer model. Their equation for LWC is given as (Forest et al., 2005):

$$LWC(z) = 1.35 H_{1/3}^2 \exp(-0.53z) \tag{2.4}$$

where $H_{1/3}^2$ is the significant wave height and z is vertical height. The liquid water content is given in units of kg m^{-3}, and is applicable for a single spray event. The work done by Forest et al. (2005) also included some other well known formulations

for liquid water content. Horjen et al. (1988) developed the following relation:

$$w = 0.1H\exp(H - 2z) \tag{2.5}$$

where w is the LWC (time averaged), H is the wave height, and z is vertical height. Roebber and Mitten (1987) cite the formulation of Brown and Roebber (1985) in a report to the Canadian Atmospheric Environment Services as:

$$w = 4.6\exp\left[- \left(\frac{2z}{H_s}\right)^2 \right] \tag{2.6}$$

where H_s is a root mean square wave height and z is the elevation above the mean sea level.

Another formulation for the liquid water content from (Zakrzewski, 1986) is:

$$w = w_o H V_r^2 \exp(-0.55h') \tag{2.7}$$

where $w_o = 6.1457$ x 10^{-5}, H is the wave height, V_r is a relative ship speed, and h' is the elevation above the deck. The liquid water content of a collision generated spray was determined to be solely a function of wave height by Kachurin et al. (1974), given below:

$$w = 10^{-3} H_w \tag{2.8}$$

Six years later, Stallabrass (1980) would modify this for his own use in deriving icing equations, giving:

$$w = 1.7 \times 10^{-4} H_w \tag{2.9}$$

It should emphasized that these previous formulations for LWC are primarily functions

of wave height. A downside in this is that it does not provide for longitudinal spray distributions across the bow of a ship (Chung et al., 1998).

A more robust study of collision generation spray was conducted by Zakrzewski (1987). That study cited various field data sets from Soviet researchers (Borisenkov and Pchelko (1975) and Kultashev et al. (1972) among others) as the basis in the development of their model to calculate spray flux for collision generated spray. This model of spray flux is a function of liquid water content, collision efficiency, relative speed of impinging droplets, and the time duration of the spraying event. The definition of the total spray flux is:

$$m = E_c U_{rs} w \Delta t_{ds} \tag{2.10}$$

where E_c is the collection efficiency, U_{rs} is the relative spray speed, w is the liquid water content, and t_{ds} is the time duration of the impinging spray. The collection efficiency used is the one formulated by Stallabrass (1980) and is discussed in Section 2.4.3. The relative speed of the impinging droplets is:

$$U_{rs} = \sqrt{U^2 + V^2 - 2UVcos\gamma} \tag{2.11}$$

where U is the spray speed, V is the ship speed, and γ is the angle between the two velocity vectors, defined by the following in three dimensions:

$$\gamma = \arccos \frac{U_x V_x + U_y V_y + U_z V_z}{\sqrt{U_x^2 + U_y^2 + U_z^2}\sqrt{V_x^2 + V_y^2 + V_z^2}} \tag{2.12}$$

The liquid water content equation used in this model is based off of the report by

Borisenkov and Pchelko (1975) and is:

$$w = w_0 \left(\frac{H}{H_0} \right) \left(\frac{V_r}{V_0} \right)^2 \exp(-0.55h') \tag{2.13}$$

where w_0 is a constant (2.42×10^{-2} kg m^{-3}), H is the wave height, H_0 is the wave height from the field data, V_r is the relative ship speed, V_0 is the velocity from the field data, and h' is the vertical elevation above the deck of the ship. Finally, the time duration of the spray event is defined as:

$$\Delta t_{ds} = \Delta t - \tau \text{s} \tag{2.14}$$

where Δt is the time duration of the spray cloud and τ is the time of the spray flight of the droplets to impact. This study was followed up by the same author shortly after, where analytical estimates for wave spray distributions across a MFV were derived (Zakrzewski and Lozowski, 1988).

2.4 Spray Droplet Trajectory and Impingement

After collision generated spray is formed with its initial vertical distribution, it then follows a trajectory path that is powered by the air flow towards the vessel or structure. Understanding the trajectory characteristics of spray following their formation is important because of its role in spray collision efficiency, and ultimately the final icing effects. The following two sections discuss two descriptions of the droplet trajectories that have been subsequently used by icing models. The first section describes the theory of water droplets being carried along streamlines in a potential flow, and the second section describes the velocity path of a droplet following a more realistic path.

2.4.1 Droplet Trajectory Following Potential Flow

Water droplets are transported and impact a ship or structure after spray generation occurs. Understanding the droplet trajectory is important because of its role in characterizing the droplet impact velocities, as well as droplet collision efficiency. One of the original, and most influential, works in droplet trajectory analysis is Langmuir and Blodgett (1946). This work was in the context of droplets impinging on aerofoils, but the physics is still applicable to sea spray droplet transport. This early modelling of droplet transport and collision was conducted in the aerospace industry, which used potential theory (inviscid, irrotational flow) to study the flow around aerofoils. The definitions for collision efficiency in a later section assume that the water droplets travel along air streamlines, until their inertia forces them to deviate and collide with an object. Since the understanding of this flow is fundamental, the definitions of the key components of potential flow (stream function and velocity potential, respectively) are given below (Lamb, 1932):

$$u = -\frac{\partial \psi}{\partial y} \qquad v = \frac{\partial \psi}{\partial x} \tag{2.15}$$

$$u = -\frac{\partial \phi}{\partial x} \qquad v = \frac{\partial \phi}{\partial y} \tag{2.16}$$

Further theoretical background in potential flows can be found in Lamb (1932) or a foundational fluid mechanics text.

Using this model in the marine icing scenario means that the spray droplets have to be assumed to be already following the air streamlines into their collision locations. That is, the following trajectory calculations do not model the trajectories of the droplets in their upward movement immediately following collision and break up.

An important aspect of the spray droplet calculations is that they are based on the droplets' presence in the wind stream lines(Yoon and Ettema, 1993). It is interesting

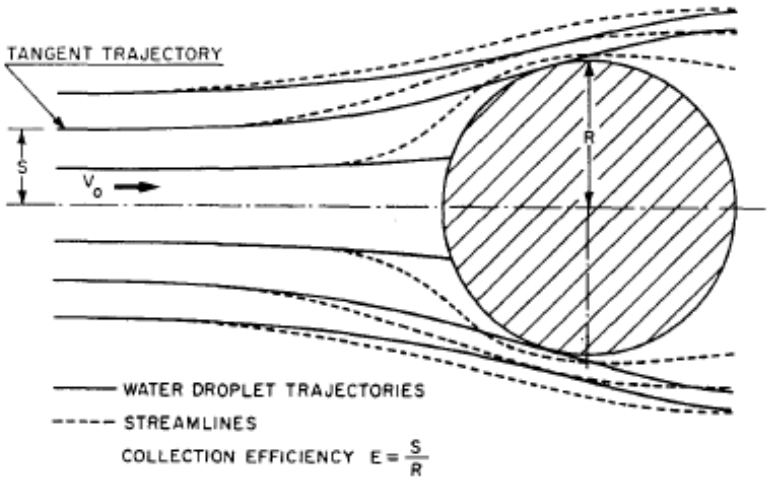

Figure 2.1: Droplet Trajectories Along Streamlines (Yoon and Ettema, 1993)

to note that Langmuir based some of his initial work from Glauert (1946), and that his improvements came from more accurate integration techniques. There are two dimensionless numbers, K and φ, derived in Langmuir and Blodgett (1946) that are useful in calculating droplet impact velocity and collision efficiency. The dimensionless numbers are defined as:

$$K = \frac{\varrho_s a^2 v}{q\eta c} \tag{2.17}$$

$$\varphi = \frac{18\varrho_a^2 cv}{\eta\varrho_s} \tag{2.18}$$

2.4.2 Droplet Movement

The path of an individual droplet can be described from a different point of view than described above. The formulation used to describe the trajectory in the marine icing

model of Lozowski et al. (2000) was based on the work of Zarlin (1980), and is defined below. Kulyakhtin and Tsarau (2014) then subsequently modified the formulation slightly by including the effects due to turbulence:

$$\frac{d\mathbf{v}_d}{dt} = -\frac{3}{4}\frac{C_d}{D}\frac{\rho_a}{\rho_w}|\mathbf{v}_d - \mathbf{U}|(\mathbf{v}_d - \mathbf{U}) - \mathbf{g}\left(\frac{\rho_a}{\rho_w} - 1\right) \tag{2.19}$$

where $\mathbf{v}_d$ is the droplet velocity, C_d is the droplet drag coefficient, D is the droplet diameter, ρ_a is the density of air, ρ_w is the density of the water droplet, $\mathbf{U}$ is the mean air velocity, and $\mathbf{g}$ is the acceleration due to gravity.

The modified form that includes the effects of turbulence in the MARICE icing model is given by (Kulyakhtin and Tsarau, 2014):

$$\frac{d\mathbf{v}_d}{dt} = -\frac{3}{4}\frac{C_d}{D}\frac{\rho_a}{\rho_w}|\mathbf{v}_d - (\mathbf{U} + \mathbf{u}_T)|(\mathbf{v}_d - (\mathbf{U} + \mathbf{u}_T)) - \mathbf{g}(\frac{\rho_a}{\rho_w} - 1) \tag{2.20}$$

where the additional turbulence effect is noted by $\mathbf{u}_T$, the turbulent fluctuation of velocity.

The drag coefficient can defined as a function of the droplet Reynolds number, Re, given by Langmuir and Blodgett (1946):

$$C_d = \frac{24}{Re} + \frac{4.73}{Re^{0.37}} + 6.24 \times 10^{-3} Re^{0.38} \tag{2.21}$$

where the Reynolds number in this case is defined as:

$$Re = \frac{2a\rho_a v_d}{\nu} \tag{2.22}$$

and a is the droplet radius, ρ_a is the air density, v_d is the droplet velocity, and ν is

the air dynamic viscosity.

It should be noted that this is a slightly modified form of the drag equation that Langmuir and Blodgett (1946) used in their analysis, where the left hand side was $\frac{C_d Re}{24}$ and defined as a function of Reynolds number. Their result was derived by fitting a curve to previously plotted empirical data points, and $\frac{C_d Re}{24}$ was used to account for the droplet's deviations from Stokes' Law.

2.4.3 Droplet Impingement

The impingement of liquid water droplets upon vessel or structure surfaces leads to a useful term, collision efficiency, that is needed in further study of marine icing. The collision efficiency is also sometimes referred to as the collection efficiency or deposition efficiency. It can be considered to be the fraction of the travelling droplets that actually impinge. That is, a collision efficiency of 0 means no droplets impinge and a collision efficiency of unity assumes all droplets impinge.

The total collision efficiency, E_M, the collision efficiency at the cylinder stagnation point, β_o, and the angle that provides for the outer limits of ice accretion can be solved as functions of the dimensionless parameters K and φ according to the Langmuir-Blodgett theory.

The collision efficiency is then defined as (Langmuir and Blodgett, 1946):

$$E_M = 0.466[\log(8K_0)]^2, \qquad 0.125 < K_0 < 1.1 \tag{2.23}$$

$$E_M = \frac{K_0}{K_0 + \pi/2}, \qquad K_0 > 1.1 \tag{2.24}$$

where K_0 is defined by:

$$K_0 = 0.125 + \frac{K - 0.125}{1 + 0.0967Re^{0.6367}} \tag{2.25}$$

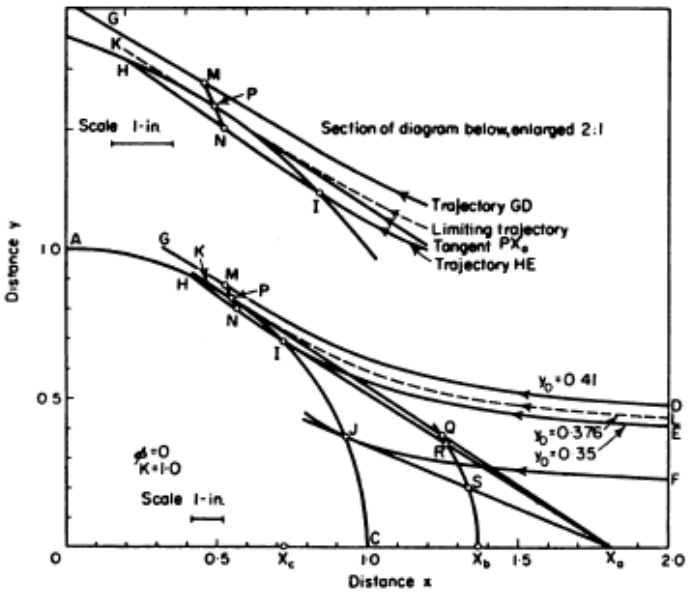

Figure 2.2: Droplet Impingement due to Deviations From Streamlines (Langmuir and Blodgett, 1946)

The process of determining E_M via tabulated values and plotted curves of K and φ, previously used by Langmuir and Blodgett (1946), was simplified by Stallabrass (1980). He defined the collection efficiency as a single parameter, ζ, which is a function of air velocity, droplet diameter, and characteristic length (cylinder diameter or body width). The parameter ζ is defined as:

$$\zeta = V^p d^q D^r \tag{2.26}$$

Stallabrass (1980) found $p = 0.6$, $q = 1.6$, and $r = -1$, giving:

$$\zeta = \frac{V^{0.6} d^{1.6}}{D} \tag{2.27}$$

The collection efficiency, E_m, is then defined for a range of $0 < E_m < 1$ (with α, β, and n constants):

$$E_m = \frac{1}{1 + \frac{\alpha}{(\zeta - \beta)^n}} \qquad \text{for} \qquad \zeta \geq \beta \tag{2.28}$$

$$E_m = 0 \qquad \text{for} \qquad \zeta < \beta \tag{2.29}$$

After Stallabrass (1980) defined the collection efficiencies in the previous two equations, he determined the values of α, β, and n by using the data first compiled by Langmuir and Blodgett (1946). The same method was also used when using the data compiled for the case of the flat plate. The collection efficiency for the circular cylinder is:

$$E_m = \frac{\zeta - 3200}{\zeta + 27000} \qquad \text{for} \qquad \zeta \geq 3200 \tag{2.30}$$

$$E_m = 0 \qquad \text{for} \qquad \zeta < 3200 \tag{2.31}$$

And the collection efficiency for the flat plate is:

$$E_m = \frac{\zeta - 2800}{\zeta + 11700} \qquad \text{for} \qquad \zeta \geq 2800 \tag{2.32}$$

$$E_m = 0 \qquad \text{for} \qquad \zeta < 2800 \tag{2.33}$$

These two definitions are important to note, primarily because the overall analysis in marine ice accretion is essentially decomposed into cylindrical and flat plate objects. Since small water droplets follow the air flow streamlines, there becomes a limit in

the validity of the previous equations; spray droplets larger than approximately 1 mm tend to have enough mass that they deviate from the streamlines moving around an object, so the collection efficiency is assumed unity.

After Stallabrass (1980) simplified the definition for the collection efficiency of spray by making a type of similarity parameter, Finstad and Lozowski (1988) took the development a step further by solving the trajectory equations used by Langmuir and Blodgett (1946) by using a digital computer. Their motivation in this was to improve the accuracy of the calculations with updated computing precision and power, and also utilized an improved equation for the coefficient of drag for a water droplet derived by Beard and Pruppacher (1969). They defined the drag coefficient of a spherical water droplet to be:

$$C_D = \frac{24}{R}\frac{D}{D_s} \tag{2.34}$$

where R is the droplet Reynolds number, D is drag force of the droplet at terminal velocity, and D_s is the drag force under Stokes flow. The ratio of D/D_s was determined empirically for a range of Reynolds numbers so that the drag coefficient could be solved, giving (Beard and Pruppacher, 1969):

$$D/D_s = 1 + 0.102R^{0.955} \qquad \text{for} \qquad 0.2 \leq R \leq 2 \tag{2.35}$$

$$D/D_s = 1 + 0.11R^{0.115} \qquad \text{for} \qquad 2 \leq R \leq 21 \tag{2.36}$$

$$D/D_s = 1 + (0.189 \pm 0.006)R^{(0.632 \pm 0.007)} \qquad \text{for} \qquad 21 \leq R \leq 200 \tag{2.37}$$

Finally, the improved collection efficiency equation, for a range of $0.17 \leq K \leq 10^3$,

given by Finstad and Lozowski (1988) is then:

$$E(K,\varphi) = [1.066K^{-6.16\times10^{\ 3}}\exp(-1.103K^{-0.688}) - 0.028] -$$
$$[(-6.37\times10^{-3})(\varphi-100)^{0.381}] \times [(3.641K^{-0.498})\exp(-1.497K^{-0.694}) - 0.045] \quad (2.38)$$

Where K and φ are the Langmuir parameters defined above.

2.5 Thermophysical and Heat Transfer Processes of Marine Icing

There are essentially two subcomponents of the overall marine icing process: i.) The spray generation, transport, and impingement of the seawater droplets; and ii.) The thermodynamics and heat transfer involved in the solidification process upon impact. Whereas the previous sections briefly described the literature pertaining to the spray, this section will discuss the freezing process that produces the final marine ice accretion. The components of several models' heat balance equations, as well as the icing governing equations will be briefly discussed.

The heat balance of the ice accretion process is most generally considered a balance between the latent heat of fusion and the convective, evaporative, radiative, and sensible heat fluxes, in the most basic sense.

2.5.1 Vessel Ice Accretion

One of the earliest works to describe vessel icing due to spray was by Stallabrass (1980). The heat balance at the surface in which icing occurs is below. It is assumed valid for medium sized fishing trawler, and to occur in steady state (Stallabrass, 1980).

$$q_f + q_w + q_c + q_e + q_a = 0 \tag{2.39}$$

Where q_f is the heat loss due to solidification, q_w is the sensible heat loss (or gain), q_c is the convective heat transfer term, q_e is the heat transfer due to evaporation, and q_s is the conduction heat transfer term. Each of the terms will be summarized below; the full derivations can be found in Stallabrass (1980). The heat loss due to solidification is given as:

$$q_f = L_f R_i \tag{2.40}$$

Where L_f is the latent heat of fusion and R_i is the rate of ice growth per unit area, for a certain freezing fraction, n, so:

$$R_i = nEwV \tag{2.41}$$

The fraction of impinging water that freezes is n, E is the collection efficiency given by Eqs. (2.30-2.33), w is the liquid water content, and V is the relative air velocity.

The liquid water content term is:

$$w = 1.7 \times 10^{-4} H_w \tag{2.42}$$

Which is a modified term given by Eq. (2.8) (Kachurin et al., 1974). The sensible heat

term, q_w, is the heat given to the supercooled water droplet upon impingement. The sensible heat term is given below, assuming the impingement surface is the equilibrium freezing temperature of water (35% salinity at -10°C) and neglecting any temperature gradient across the water film runoff.

$$q_w = R_w c_w (t_d - t_s) \tag{2.43}$$

Where $R_w = EwV$, c_w is the specific heat of the water droplet (∼4000 J/kgC), t_d is the droplet temperature immediately before impact, and t_s is the equilibrium temperature.

Next, the convective heat transfer term is given as:

$$q_c = h(t_a - t_s) \tag{2.44}$$

Where h is the convective heat transfer coefficient, and t_a and t_s and the temperatures of air are the surface, respectively. The heat transfer coefficient can be defined as an approximation, for both the case of the flat plate and cylinder, assuming roughness effects, turbulence, and a mean film boundary layer air temperature of -5°C as:

$$h = 5.17V^{0.8} \tag{2.45}$$

Where V is the air stream velocity and the characteristic length is assumed to be 3 m. Combining, the convective heat transfer term is then:

$$q_c = 5.17V^{0.8}(t_a - t_s) \tag{2.46}$$

The evaporative heat transfer term can be solved by using an analogous form of the

convective heat transfer term. Solving and simplifying gives the solution below, where e_a and e_s are the saturation vapour pressures of moist air at t_a and t_s.

$$q_e = 89.5(e_a - e_s)V^{0.8} \tag{2.47}$$

Also Stallabrass (1980) included the conduction heat transfer term in the original heat balance, it was a largely notional input. This term is typically ignored, but does become relevant if there is inadequate insulation in ship cabin spaces, which would allow a temperature gradient across the wall. Finally, by combining the previous heat balance terms, with $L_f = 3.33 \times 10^5$ J/kg, the icing rate is (kg/m^{2}s):

$$R_i = 2.04 \times 10^{-6} H_w V(t_s - t_d) + 1.55 \times 10^{-6} V^{0.8}\{(t_s - t_a) + 17.3(e_s - e_a)\} \tag{2.48}$$

The follow on work of the laboratory scale spraying experiments of Chung et al. (1998) consisted of a three dimensional model of the icing of a specific vessel, the Canadian fishing trawler *Zandberg* (Chung and Lozowski, 1998). The unique part of this work is that it is the only known model in the literature that is based on laboratory scale experiments in ship spraying in an effort to better understand marine icing. The way these two works were integrated is that the experimental data of the spray flux from Chung et al. (1998) was used as a basis for the input data for(Chung and Lozowski, 1998). Furthermore, the spray flux was specified both vertically and longitudinally across the surface of the vessel. The model then takes the input distribution of spray and then calculates the extent of icing that occurs. The incoming time averaged spray flux density was experimentally derived to be, for full scale:

$$m'(x, y) = kV_s^3 H_{1/3}^7 e^{\alpha + \beta(x - x_{hull})} \tag{2.49}$$

where:

$$\alpha = -0.5009 - 0.2797y^2 + 2.2423 \times 10^{-3}y^3 \tag{2.50}$$

$$\beta = -0.2489 - 0.0206y^2 + 2.9796 \times 10^{-3}y^3 \tag{2.51}$$

and the time averaged spray flux density is m'(x,y) (kg m^{-2}s^{-1}), and x and y are the full scale dimensions of the ship, taken from the bow and centerline, respectively. Also, k is the proportionality constant (2.85 $\times 10^{-7}$ kgs^{2}m^{-12}), V_s is the ship speed (2.5 to 8.0 m s$^-$1), and $H_{1/3}$ is the significant wave height (2.5 to 5.0 m, full scale). The model tests were executed at a scale of 1:13.4. Once the magnitude of the incoming spray flux is known, the model calculates the distribution of the droplets across the vessel by taking the wind drag's influence into effect. The trajectory equation used is similar in form to the one used by Zarlin (1980), above. The wind velocity is assumed uniform in the vertical direction, and no influence of ship components on the flow is considered. The spray field droplet distribution is assumed to only vary in the vertical direction upon formation, and to be of uniform diameter of 1.75 mm in accordance Zakrzewski (1987). Once the total incoming spray mass and distribution is known, the thermodynamics and freezing process can be calculated. Assuming the collision generated water droplets are ejected at the sea surface temperature and supercooled to the air temperature, its cooling equation is given by:

$$\frac{dT}{dt} = \frac{6}{d\rho_b C_b}\left[h(T - T_a) + h\left(\frac{Pr}{Sc}\right)^{1/3}\left(\frac{0.622L_e}{C_p P_a}\right)(e_s(T) - RHe_s(T_a)) + \sigma(T^4 - T_a^4)\right] \tag{2.52}$$

where T is instantaneous temperature of the water droplet, d is the droplet diameter, ρ_b is the droplet density, C_b and C_a are the specific heat capacities of the droplet and air, respectively, h is the convective heat transfer coefficient, T_a is the air temperature,

Pr is the Prandtl Number, Sc is the Schmidt Number, Le is the specific latent heat of vaporization of water, $e_s(T)$ and $e_s(T_a)$ are the equilibrium vapour pressures of the droplet and pure water, respectively, RH is the relative humidity, and σ is the Stefan Boltzman constant. The balance of the heat lost from the liquid brine film to the air ultimately gives way to the icing rate. The heat balance in this model is given as:

$$q_f + q_s = q_c + q_e + q_r \tag{2.53}$$

where the terms in the above equation are the latent, sensible, convective, evaporative, and radiative heat fluxes ($\mathrm{W/m^2}$). The convective, evaporative, and radiative heat fluxes are given in a similar form as Eq. (2.45), albeit with a different value of h. The sensible heat flux in warming the brine flux, m_b, to the equilibrium freezing temperature, T_s, is:

$$q_s = m_b C_b (T_i - T_s) \tag{2.54}$$

The latent heat of freezing heat flux that includes the term $\frac{dL}{dt}$, the icing rate ($\mathrm{kg{\cdot}m^{-2}{\cdot}s^{-1}}$), is finally:

$$q_f = (1 - \lambda) L_f \frac{dL}{dt} \tag{2.55}$$

Where λ is the liquid fraction of the spongy ice and L_f is the latent heat of solidification of pure water ($\mathrm{J{\cdot}kg^{-1}}$).

2.5.2 Marine Icing of Offshore Structures

This section will briefly review two of the major marine icing models of offshore structure, ICEMOD and RIGICE, and touch on a new model, MARICE. The first two models were created in the 1980s in Canada and Norway, respectively, and have

been updated and refined since (Roebber and Mitten, 1987; Brown and Horjen, 1989; Forest et al., 2005). The primary motivation for the creation of these models was the expansion of the offshore petroleum industry's increased operations in the higher latitudes that have harsh winter weather. Although the spray generation and causes of vessel icing can be somewhat different than structure icing, the underlying physics of the their icing processes are similar. Because of that, the discussion of structure icing is relevant to the bigger picture of this review.

Major differences between ICEMOD and RIGICE are that ICEMOD is time dependent and includes computations for both cylinders and flat plates, which make up the overall structure. RICICE has assumptions of steady state icing and only considers cylinder shapes. The governing equations for icing in the ICEMOD model are below, with the heat balance equation following (Brown and Horjen, 1989):

$$L(X) = R_w + \dot{m}_e - R \tag{2.56}$$

$$C_b X \frac{D\Theta_b}{dt} = \dot{Q}_s + L_f R + \dot{Q}_i \tag{2.57}$$

$$X \frac{DS_b}{dt} = R_w S_w - S_b[R_w + \dot{m}_e - R(1-\sigma)] \tag{2.58}$$

where X = $\rho_b \delta$ (ρ_b = density of brine film, δ = brine film thickness), R_w is the local water catch rate, $\dot{m}_e$ is the mass transfer rate due to evaporations, R is the local icing intensity, C_b is the specific heat capacity of the brine film, Θ_b is the temperature of the brine film, $\dot{Q}_s$ is the net heat flux at the brine film interface, L_f is the latent heat of fusion of the saline ice, $\dot{Q}_i$ is the heat flux through the ice (neglected in computation), S_b is the salinity of the brine film, S_w is the salinity of the impinging water, and σ is

the interfacial distribution coefficient (S_i/S_b). Furthermore, the mean value across the brine film is defined by:

$$(\cdot)_b = \frac{1}{\delta}\int_0^{\delta}(\cdot)\mathrm{d}n \tag{2.59}$$

and the operator L( ) is defined by:

$$L(\cdot) = \frac{\partial(\cdot)}{\partial t} + \nabla_t \cdot [(\cdot)\vec{v}_b] \tag{2.60}$$

The heat balance across the air/brine film boundary is then:

$$\dot{Q}_s = \dot{Q}_c + \dot{Q}_e + \dot{Q}_w + \dot{Q}_r + \dot{Q}_v \tag{2.61}$$

where $\dot{Q}_s$ is the net heat flux across the film interface, $\dot{Q}_c$ is the sensible heat flux, $\dot{Q}_e$ is the evaporative heat flux, $\dot{Q}_w$ is the heat transfer between the impinging spray and liquid film, $\dot{Q}_r$ is the heat transfer due to radiation, and $\dot{Q}_v$ is the the heat transfer due to the compression of air and the viscous effects in the air boundary layer. Full derivations of the previous heat fluxes can be found in Appendix A of Brown and Horjen (1989). Ultimately, the second "icing equation", is defined as:

$$L(Y) = R_w S_w - \sigma R S_b \tag{2.62}$$

where Y=S_bX. Interestingly enough, the impinging spray flux calculation deviates from the field of thought used by Langmuir and Blodgett (1946) and Stallabrass (1980). In this case, the collision generated spray flux is derived from Norwegian field measurements on their offshore rigs.

The MARICE model separates its calculations into two regimes of the structure, with the lower regime calculating saline marine icing and the higher regime focussing solely

on atmospheric icing (Roebber and Mitten, 1987). The following summary will only look at the marine icing effects. The heat balance modelled for a circular cylinder is given by:

$$Q_f + Q_v + Q_a + Q_h = Q_c + Q_e + Q_l + Q_s \tag{2.63}$$

where Q_f is the latent heat released during freezing, Q_v is the frictional heating of air, Q_a is the heat released in cooling accreted ice from its freezing temperature to the surface temperature, Q_h is the artificial heating of the surface, Q_c is the sensible heat loss to air, Q_e is the evaporative heat loss, Q_l is the heat loss in warming the water drops to the freezing temperature, and Q_s is the radiative heat loss. For the sake of brevity, the full derivations for the previous terms can be found in Roebber and Mitten (1987). The brine run off due to salinity effects and wet growth formation of spongy ice is included in the model by a sponginess factor:

$$\chi = 1 - \frac{S_i}{S_b} \tag{2.64}$$

where s_i is the salinity of the ice and s_b is the brine salinity. The salinity of the brine is then defined, with T_F being the freezing temperature:

$$S_b = \frac{-T_F}{0.054} \tag{2.65}$$

Finally, the freezing fraction n can be defined as:

$$n = \frac{S_b(T_F) - S_w}{\chi S_b(T_F)} \tag{2.66}$$

The icing can then be calculated iteratively from the previous governing equations - the iteration steps are fully explained in Roebber and Mitten (1987).

Chapter 3

Experimental Methods

3.1 Introduction

This chapter will overview the approaches taken in carrying out the experimental trials during this thesis. The experimental objectives will first be laid out in Section 3.2. The broad scope of the objectives will also be given in the context of the previous literature review, showing its relevance and research merit. Details of the laboratory facilities where the experiments were conducted will then be discussed. The necessary development and fabrication of the test models will follow, along with outlining the specifications and use of the measurement devices operated. The error analysis and uncertainty estimates associated with the experimental system will be calculated next. Finally, the methodology used to carry out the experiments will be explained.

3.2 Experimental Objectives

The primary experimental objectives of this thesis were the design and development of a system to obtain laboratory scale experimental data of collision generated spray in the context of marine icing research. Requisite subtasks were surveying the

literature investigating the marine icing field, developing a working knowledge of laboratory tow tank operations and previous marine icing experiments, and fabricating multiple test models for experimental trials. More specifically, the behaviours and characteristics of the spray generation such as droplet sizes, quantities, and velocities can be useful in understanding spray formation in the lab in reference to marine icing. A secondary objective is to provide experimental data to serve as validation for follow on computational research to be conducted. To this end, impact pressures of the oncoming waves are measured as part of the validation data. These experiments fit into the context of the previous research in the literature by attempting to develop a greater understanding of the conditions and behaviours of the spray generated LWC contributing to icing, albeit at the laboratory scale.

3.3 Laboratory Facilities and Measurement Tools

The experimental tests were conducted in the Ocean Engineering Research Centre (OERC), Memorial University of Newfoundland Faculty of Applied Science and Engineering. Model fabrication was conducted in the Memorial University of Newfoundland Department of Technical Services in conjunction with assistance by laboratory technicians in the OERC. The largest and most important facility in conducting experiments was the facility's tow tank, which was used for its wave making capabilities. The technical specifications of the tow tank and interfaced measurement tools are detailed below, which include test models, wave probes, a high speed camera, pressure sensors, an ultrasonic sensor, and data acquisition.

3.3.1 Tow Tank

The tow tank in the OERC was instrumental to this thesis and served as the basis for all tests' execution. Its physical specifications are documented in a tow tank schematic located in the control room of the OERC (Figure 3.1). It has a length of 57.4 meters, width of 4.57 meters, and a maximum water level of 3.04 m. The water level is typically maintained at ∼2 meters, however, but can be adjusted to higher or lower levels as needed. Waves are generated by a single paddle board style wave maker, which is powered by a single 3,000 PSI, 125 hp hydraulic drive. The opposite side of the tow tank contains a wave dampening beach that limits the actual usable tow tank

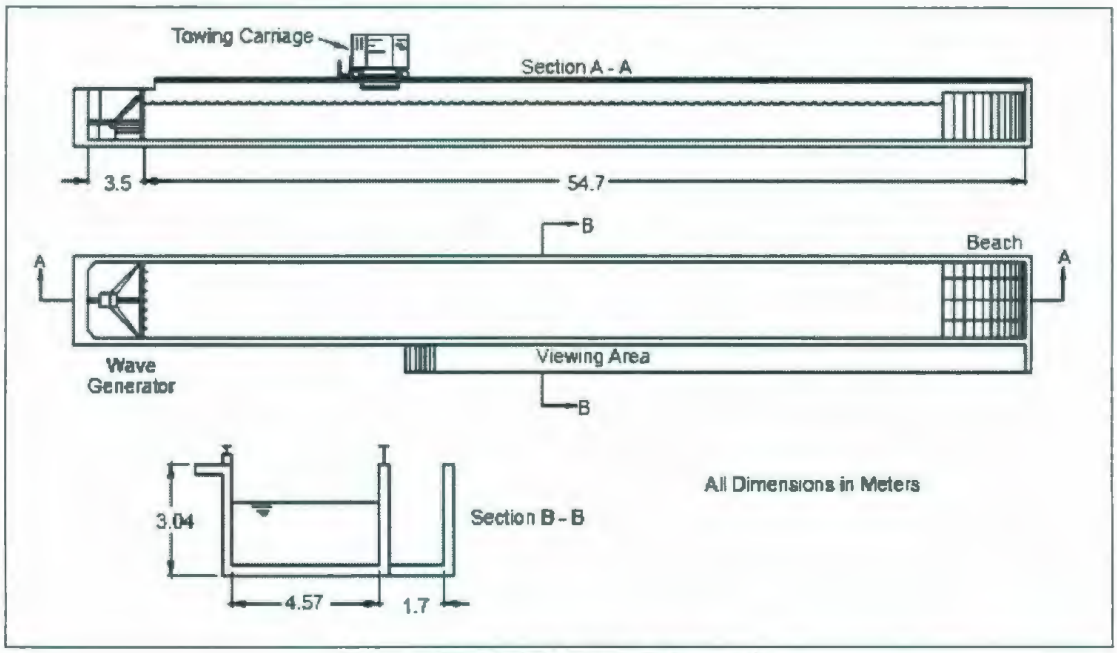

Figure 73: MUN Tank Schematic
Figure 3.1: Tow tank Schematic (OERC)

6.2 Test Instrumentation

Towing Dynamometer

The towing dynamometer used was a *Kempf & Remmers* R 47 resistance dynamometer. The balance contains a load cell which has a rating of ±50lbs (approximately ±220 N). It

percent of the total span travelled. The total span is defined by the length of the hydraulic drives full range of motion of 2 feet. Computer software allows for further robustness by providing the ability to generate random waves, or waves specified by a certain wave frequency spectrum. This is used to simulate the behaviours of realistic sea waves for a variety ship model testing needs. The tow tank also houses a tow carriage which holds test models, and can either remain stationary for testing or move along the tow tank. The maximum forward velocity of the tow carriage is 5 m/s. The tow carriage held the test models stationary for the purposes of this thesis at approximately at the midway point of the tank. This location was chosen for largely for two reasons; 1) it was conveniently located in front of the control room which provided ease of access to the carriage, and 2) it was in line with a glass window at the free surface. The glass observation window below the control room located at the water free surface and provides unobstructed views to test models from a horizontal, perpendicular orientation.

3.3.2 Test Models

The creation of test models posed some initial problems that had to be overcome. Ideally, an actual scale model ship hull should be used in the tow tank to induce the spray that would then be studied, as in Chung et al. (1998). Initial feasibility study tests were conducted using a pre-existing ship hull model (Figure 3.4), which is currently maintained and operated by the laboratory technicians in the OERC. Several initial tests were conducted with this model and it was determined that this ship hull model was not an appropriate test model for this thesis. This was largely due to the required high forces associated with spray generating waves that would be

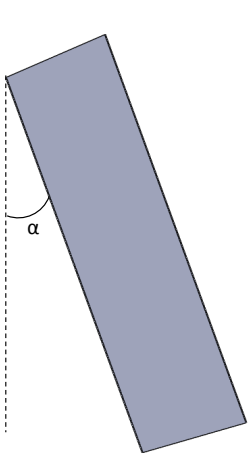

(a) Variable Vertical Angle

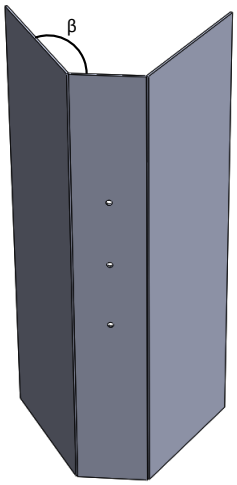

(b) Variable Side Angles

Figure 3.2: Angular Variations of Test Model

excessive for this particular set-up. Ultimately, since spray could not be created with the wave/model collision using the realistic, previously constructed ship hull model, it was determined that several different models had to be designed and fabricated.

Figure 3.3: Scale Vessel Model

The development of the newer models had to keep strength and rigidity as primary concerns due to the high wave energies required to create spray. The other priority was to create lab scale models that had variations, and approached a somewhat simplified,

mock simulation of a ship hull. The first model created was both the simplest, and easiest to induce spray - a flat plate. It was also constructed in an initial effort to generate spray and establish test and measurement procedures. The model was 39.5 inches tall, 28 inches wide, and had angled 8 inch sides on the left and right of the model which aimed to guide incoming water around the model edges. The model was fabricated from 3/16 inch aluminum and was attached to the tow carriage with a pre-existing piece that is used for water/structure interaction labs. Inherent in the flat plate's large frontal surface area is the high impact force and applied moment. Additional metal beams were required to clamp the model to the tow carriage in an effort to minimize model movement during impact. The actual experimental iterations conducted will be detailed below.

The second model created started to approach more approximate shapes of a ship hull (Figure 3.3). It had a narrower front face and was created to be capable of hanging from the tow carrier at an angle (α) with respect to the vertical axis and to have side plates of variable angle (β). The experimental trials were conducted for a total of three different configurations for this model, and are detailed below. The three different configurations: 1) $\alpha = 0°$, $\beta = 120°$, 2) $\alpha = 0°$, $\beta = 135°$, and 3) $\alpha = 0°, 20°$, $\beta = 135°$. The specific test runs and execution of the experimental trials will be further discussed below.

3.3.3 Wave Probes

The wave height was measured by using Akamina model AWP-24 capacitive wave probes. The wave probes work by having a support structure containing a 50 cm long capacitive wire placed into the water. The capacitive wire can measure the wave

height by detecting the change of the system capacitance as water surface elevation changes. Three wave probes were used for the first and second model configurations and two were used for the third configuration. They were placed such that the far field wave height, the wave height at the point of impact, and the wave reflection after impact could be measured. The last position was omitted because the narrower face limited probe placement. Important data that can be obtained directly from the wave probe data files include wave height and wave period. The wavelength can be calculated once the wave period is known. The wave steepness can be calculated by using the values of the wave height and wavelength.

3.3.4 High Speed Camera

Imaging was acquired through the use of a high speed camera. The purpose of this was to obtain data that could be used in the analysis of the spray formation by both qualitative and quantitative methods. Initial troubleshooting tests were conducted with an older Mega Speed model MS55K S2 high speed camera. A newer, modern Phantom V611 high speed camera was acquired for use amongst the Marine Icing Research group and other collaborating groups and was justified by its higher performance (better resolution, sharper image, faster frame rate, etc.). This model is capable of an image acquisition speed of 6242 fps at a maximum resolution of 1280 $\times$ 800 pixels. Furthermore, its maximum image acquisition speed can bet set to 1,000,000 fps at a 1280 $\times$ 8 pixel resolution. The exposure rate can also be set from within a range of 1 μs to 300 ns. The camera was placed in two positions in relation to the test model, and two vertical viewing perspectives for each position. The two positions used were a side view and frontal view of the model, and the vertical positions enabled

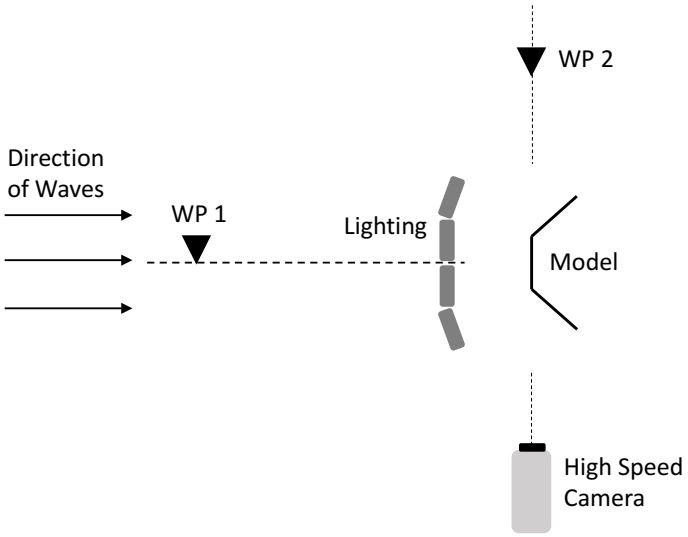

Figure 3.4: Experimental Set-Up

the camera to view both the lower elevation sheet breakup and the higher elevation spray trajectory. Bright lighting was also necessary for the camera to obtain adequate imaging. Bright lighting (mostly LED) was placed directly in front of the model, and two LED lights were attached to the tow carriage above the model.

3.3.5 Pressure Sensors

The pressure sensors used were Nova Sensor model NPI-19 medium pressure sensors. Each sensor contains a piezoresistive sensor chip inside a hermetically sealed diaphragm housing. External threading allowed the sensors to be flush mounted to the model test rigs. The purpose of these sensors was to measure the impact pressure, P, of the oncoming waves. The data from these sensors is ultimately to be used as experimental validation for another student's computational predictions. The particular sensors in this application were chosen based off of previous research that investigated impact pressures of waves onto a body (Fullerton et al., 2010). Although the sensor face side

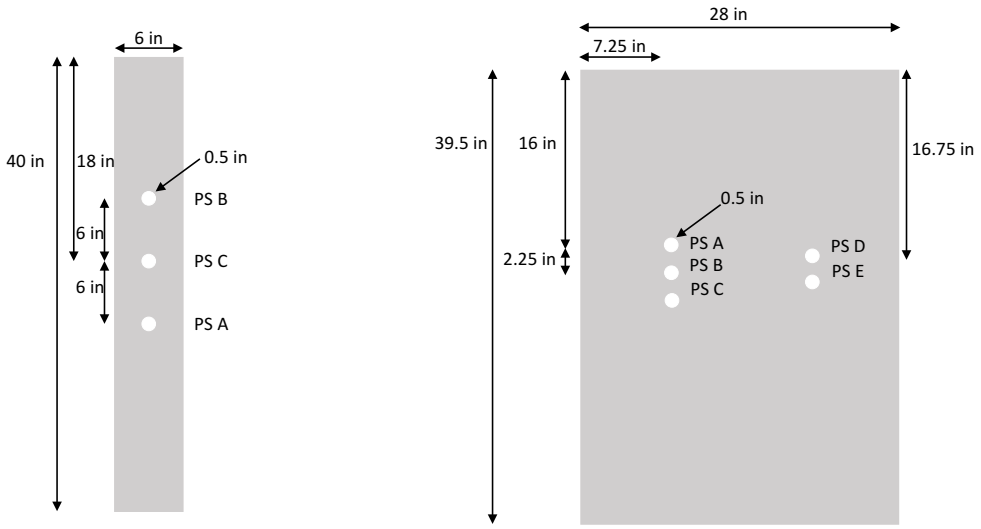

(a) WP1

(b) WP2

Figure 3.5: Pressure Sensor Positioning

is waterproof, the backing is not. The sensors were then waterproofed by sealing and encasing the rear of the sensor in epoxy. The sensors were placed into position such that the lowest sensor was close to the top of the water surface, and not submerged. The relative locations of the pressure sensors are illustrated in Figure 3.6.

3.3.6 Ultrasonic Sensor

A Senix brand ultrasonic sensor was chosen for use during the initial feasibility and troubleshooting trials on the flat plate model. This sensor was unfortunately not fully utilized for the entirety of the experimental trials, but should still be mentioned. An ultrasonic sensor is a sensor that uses sonic pulses to measure distance from the sensor. The intent of this sensor was to measure the time evolution of the horizontal distance of the incoming wave to the model wave. The use of this sensor was also motivated by the successful results from Fullerton et al. (2010).

3.3.7 Data Acquisition

Data from each wave probe and pressure sensor was acquired by using a National Instruments model NI cDAQ-9178 that was interfaced with National Instruments LabVIEW Signal Experss software. A regulated DC power supply was used to provide necessary excitation voltage for the sensors. A 10 VDC voltage source was given to the pressure sensors and wave probes as the excitation voltage. The output voltages were interfaced into the input pins of the DAQ, and wiring colour coding was used for the different pressure sensors to maintain correct records. Data from the pressure sensors and wave probes were both recorded on the same LabVIEW project files, so the sensor signals were synchronized with respect to time. The data was recorded at 2 kHz for each model except for the last configuration of $\alpha = 0^o, 20^o$ and $\beta = 135^o$. The final sample rate was set to 10 kHz in an effort to prevent a noisy signal as experienced with the prior trials. It was eventually determined that the source of the noise was likely some of the remaining 60 Hz alternating current voltage being input into the DC power regulator. Using digital filtering settings in LabVIEW enabled the signal to be recorded with less noise than in prior trials. Matlab was utilized to conduct signal conditioning of the initial recordings by using the Savitzky-Golay filtering function "sgolayfilt".

The imagery data was collected with the proprietary Phantom Camera Control software, as opposed to directly with LabVIEW. The camera has a variety of settings that can be used to obtain the desired image characteristics. The most influential settings are the image resolution, frame rate, and exposure rate. Changing resolution affects the window size of the image, and ultimately the sharpness and precision of the image. Increasing the frame rate is useful in fast moving processes and can both

decrease the step size of the image capture rate and blurring effects that may happen. Exposure time has traditionally been controlled by a mechanical shutter opening and closing, but this camera utilizes digital control. A faster exposure rate would mean that the shutter is open for less time, resulting a darker image and a need for more lighting. The camera setting for most trials was set to recording at 1024x768 pixels, 1000 fps, and 400 μs exposure time. Some minor deviations did occur, mainly due to lighting issues.

3.4 Measurement Calibration

The calibration of the tow tank is conducted periodically by the lab technicians in accordance with the International Towing Tank Conference (ITTC) industry standards. The tow tank calibration ensures that the wave board span and frequency set points, as controlled by the digital controller, are accurate and that the wave amplitudes are generated accordingly. Unfortunately, the actual data files proving calibration were not obtained. The tow tank calibration procedures have been on schedule and in accordance with applicable regulations, however, previous documentation could not be acquired for this thesis.

The wave probes, pressure sensors, and high speed camera were also calibrated prior to use to ensure proper measurement techniques. Each wave probe was calibrated using an external water tank and known distances. A best fit equation was input into NI LabVIEW Signal Express for the wave probes' data acquisition. This was also conducted by the lab technician in the standard method used in the lab. The pressure sensors were initially calibrated by using a manufacturer calibrated pressure transducer

(a) Vertical Example (b) Tilted Example

Figure 3.6: Checker Board Camera Calibration

(Omega model PX-603) as a reference against a common pressure source for several measurements and creating a best fit curve of the data points. Sensor linearity was also confirmed for its range. Comparing the pressure sensor initial results to both Fullerton et al. (2010) and Greco et al. (2012) showed similar pressure magnitudes for similar wave impact characteristics. The camera calibration was conducted by taking images of a black and white square checker board of known and uniform width (30 mm). The checker board image was placed in the focal plane of the camera and positioned in several different locations and orientation. Some example images are shown in Figure 3.7. The purpose of this calibration is to define the proper correlation of model spatial dimensions to pixels (mm/pixel, for example) that can be used in the image post processing.

3.5 Uncertainty Analysis

This thesis would be remiss without a discussion on the measurement errors and uncertainties encountered in the execution of the experimental trials. Measurement errors and uncertainties are natural by-products of using instruments to experimentally

obtain data. Ultimately, there is a difference between the recorded measurement value and the true value, known commonly as the measurement error. The uncertainty can be thought of as an estimate of the overall error due to all sources of imprecision or bias. This can be described mathematically by the following relation for a measured parameter X_i (Moffat, 1988).

$$X_i = X_i(\text{measured}) \pm \delta X_i \tag{3.1}$$

The overall uncertainty of the measured parameter is denoted by δX_i, and is comprised of two types of error. These two types are the precision error and the bias error. The precision error contains errors that are random in nature, and the bias error is a constant, fixed contribution. Sources of bias error typically can be seen in calibration error, sensor hysteresis, or even an experimentalist's misreading of a gauge. The precision error is a statistical approximation used for predicting ranges of measured values, typically within a 95% confidence interval. The precision error can be calculated as twice the standard deviation of a set of observations, or 2σ. Finally, the total uncertainty can be defined as function of both the precision and bias errors (Kline and McClintock, 1953; Moffat, 1988).

$$U_{X,i} = [P_{X,i}^2 + B_{X,i}^2]^{1/2} \tag{3.2}$$

Analysis of the overall uncertainty of a result R can be calculated by the propagation of its components' precision and bias error, where the measurement of each component is independent with an assumed 95% confidence interval. The formulation for the

overall error uses the root-sum-square method by Kline and McClintock (1953) below.

$$\delta R = \left\{ \sum_{i=1}^{M} \left(\frac{\partial R}{\partial X_i} \delta X_i \right)^2 \right\}^{1/2} \tag{3.3}$$

The result R is commonly a function of measurements that are products, such as a fluid's Reynolds number. For a result $R(X_1^a, X_2^b, \ldots, X_M^m)$, a generalized formulation for the propagated error can be derived by rearranging Eq. (3.3).

$$\frac{\delta R}{R} = \left\{ \left(a \frac{\delta X_1}{X_1} \right)^2 + \left(b \frac{\delta X_2}{X_2} \right)^2 + \cdots + \left(m \frac{\delta X_M}{X_M} \right)^2 \right\}^{1/2} \tag{3.4}$$

3.5.1 Measurement Error

An estimate of the measurement error for the sensors used can be determined through the relations above. The precision error for the pressure sensors and the wave probes was calculated by first recording values when the overall data acquisition system was running in normal conditions. Forty one measurements were taken for the pressure sensor error and thirty one were taken for the wave probe. The importance of using this method to calculate the precision error is that it absorbs the random errors associated with the entire system running, instead of just the imprecision of the instruments themselves. The bias error is considered a fixed error and can arise from several sources typically, such as offset or in imperfect calibration settings. The bias errors were assumed to be an estimate of 0.5%, representing the "fossilized" error that is retained after sensor calibration (Kim and Simon, 1993). An additional method of alleviating a fixed error for the impact pressure measurement was to normalize the ambient pressure to zero, thus calculating the impact pressure as the peak (maximum)

value of the impact reading.

The repeated measurements taken during normal operating conditions are typically taken prior to the start of an experiment. This was unfortunately not conducted, so the equivalent measurements are taken from trial runs before impact, and after start up. This could explain the relatively large precision error for the wave probe reading of water surface elevation if the water level was not perfectly calm at the start of each trial. The tabulated values for the measurement errors are located in Table 3.1.

Instrument	Precision Error (%)	Bias Error (%)	Uncertainty (%)
Pressure Sensor	0.974	0.5	1.095
Wave Probe	4.697	0.5	4.724

Table 3.1: Measurement Errors

3.5.2 Propagated Uncertainty in Results

The overall uncertainty estimates, comprised of the measurement precision and bias errors, can be calculated by following the procedure laid out by Kline and McClintock (1953) and in accordance with the estimation reporting policy of the Journal of Heat Transfer (Kim and Simon, 1993). The calculated results that have errors propagated through them are the wave period, wavelength, and wave steepness.

The calculation of the wave period can be taken directly from the data and plot of the water wave heights. The wave period , T_w, can be considered the distance between two peaks of a wave. This distance can be calculated with MATLAB by subtracting

the differences in x-axis (time, t) positions of each peak, given by:

$$T_w = t_{peak,2} - t_{peak,1} \tag{3.5}$$

The uncertainty due to the period readings can be attributed to the resolution of the x-axis, which is the time step of the data acquisition ($\Delta t = 0.0001$ s). The precision error of the period can therefore be estimated by Equation (3.6). The bias error, B_{T_w}, is again assumed to contain approximately 0.5% error, ensuring conservative estimates in error.

$$P_{T_w} = [(\delta t_{peak,2})^2 + (\delta t_{peak,1})^2]^{1/2} \tag{3.6}$$

The wavelength is given by Bhattacharyya (1978) as $L_w = gT_w^2/2\pi$, and its precision and bias errors can be can be calculated by following Eq. (3.4) above.

$$\frac{P_{L_w}}{L_w} = \left\{ \left(2\frac{P_{T_w}}{T_w} \right)^2 \right\}^{1/2} \tag{3.7}$$

$$\frac{B_{L_w}}{L_w} = \left\{ \left(2\frac{B_{T_w}}{T_w} \right)^2 \right\}^{1/2} \tag{3.8}$$

The uncertainty of the wave period is then propagated into the uncertainty of the non-dimensional value of wave steepness, $k = H_w/L_w$, following the same procedure.

$$\frac{P_k}{k} = \left\{ \left(\frac{P_{H_w}}{H_w} \right)^2 + \left(\frac{P_{L_w}}{L_w} \right)^2 \right\}^{1/2} \tag{3.9}$$

$$\frac{B_k}{k} = \left\{ \left(\frac{B_{H_w}}{H_w} \right)^2 + \left(\frac{B_{L_w}}{L_w} \right)^2 \right\}^{1/2} \tag{3.10}$$

The total contributions of the precision and bias errors to the overall uncertainty estimate can be calculated by using Equation (3.2). The overall estimates of propagated uncertainty are located in Table 3.2.

Result	Precision Error (%)	Bias Error (%)	Uncertainty (%)
Wave Period	0.013	0.500	0.517
Wavelength	0.026	1.000	1.033
Wave Steepness	4.697	0.707	4.750

Table 3.2: Overall Experimental Uncertainty Estimates

3.6 Procedure and Experimental Methodology

Several different iterations of the same procedure occurred during the course of this thesis work. The repetition was due to the different model shapes that were previously discussed. The first step was to ensure proper calibration and set up of the measurement devices described above. The test rig was then lowered into position and securely bolted to a support structure, which was clamped to the frame of the tow carrier. The metal support structure was previously used in undergraduate Fluid/Structure Interaction labs and was reused for all trials conducted. The stability of the flat plate model was improved as previously discussed. Next the camera and its associated lighting was put in place. Two LED lights were installed vertically above the model and directly in front of the model were two LED lights and a halogen work light. This combination seemed to provide adequate lighting for the camera and no noticeable flickering occurred due to alternating current. The camera was then positioned in either the side or frontal position along with the desired perspective of sheet break up or spray trajectory set in the camera focal plane. This was conducted fully in all perspectives for the flat plate model and the model set to $\alpha = 0°$ and $\beta = 120°$. The spray perspective from the side position was not captured for the latter case due to time constraints in the lab. The model set to $\alpha = 0°, 20°$ and $\beta = 135°$ was viewed from the side looking at the spray. The same model was also viewed from the

front for a limited range of frequencies and spans when $\alpha = 20°$. This was again due to unforeseen laboratory time constraints imposed. Finally, experiments were then conducted once the test rig was installed in place, with its pressure sensors mounted, wave probes installed, and the camera and lighting were set up.

Ideally, the planning and execution of experimental trials should follow the theory of the Design of Experiments (DOE), which has been refined over the past century. The idea behind this is to avoid unnecessary trials and to also have a systematic and statistically robust method of experimentation (Fisher, 1966; Montgomery, 1997). The initial experimentation deviated somewhat from this philosophy in its execution, primarily due to a lack of published experiments of this type. The upper and lower bounds of the wave frequency and wave maker span were determined from a sort of trial and error method, guided by the experience of the lab technician. This then served as a basis for choosing the most appropriate frequency and span values for the flat plat model and the second model ($\alpha = 0°$; $\beta = 120°$).

Test matrices that show each wave frequency and wave board span selected for each configuration are shown below. Three iterations per test run were conducted to ensure sufficient statistical robustness. The summary tables are shown in Table 3.3 - 3.7.

The software package Design Expert 9.0 was employed to design the test runs for the final configurations for the side perspectives of $\alpha = 0°, 20°$ and $\beta = 135°$. The best spray inducing frequencies and spans from the initial trials were selected and input into the software as a two factorial design for each model configuration, with two iterations per frequency/span combination. A range of five frequencies and spans were selected, ranging from 0.80-1.0 Hz and 35-55% in 0.05 Hz and 5% increments. Two repetitions instead of three were chosen purely due to time constraints. Unforeseen

Frequency (Hz)	Span (%)
0.95	50
0.85	50
0.95	40
0.95	45
0.85	50
0.85	45
1.00	35
1.00	40

Sheet Perspective

Frequency (Hz)	Span (%)
0.95	50
0.85	50
0.95	40
0.85	50
0.85	45
1.00	35
1.00	40

Spray Perspective

Table 3.3: Flat Plate Test Matrix (Side Position)

Frequency (Hz)	Span (%)
0.95	50
0.85	50
0.95	40
0.95	45
0.85	45
1.00	35
1.00	40

Sheet Perspective

Frequency (Hz)	Span (%)
0.95	50
0.85	50
0.95	40
0.95	45
0.85	45
1.00	35
1.00	40

Spray Perspective

Table 3.4: Flat Plate Test Matrix (Front Position)

scheduling delays in the lab cut these experimental trials short by a considerable amount ($\sim 45\%$). The test matrix created for these tests is located in Table 3.4. The test runs for the final frontal view were abbreviated, so only several of the better combinations from the previous trials were chosen.

Frequency (Hz)	Span (%)
0.95	50
0.85	45
0.95	50
0.95	40
1.20	20
1.20	25
1.20	30
1.00	35
1.00	40
0.95	45
1.10	35
0.85	55

Sheet Perspective

Frequency (Hz)	Span (%)
0.95	50
0.85	45
0.85	50
1.00	35
1.00	40
0.95	45
0.85	55
0.80	55
0.90	55
0.75	55
0.80	60
0.50	80
0.70	65

Spray Perspective

Table 3.5: 120° Model Test Matrix (Front Position)

Frequency (Hz)	Span (%)
0.85	45
0.95	50
1.00	35
1.00	40
0.85	55
0.90	55
0.80	55

Table 3.6: 120° Model Test Matrix (Side Position, Sheet Perspective)

Frequency (Hz)	Span (%)
0.85	50
0.80	45
0.90	45
0.85	35
0.80	50
0.80	55
0.90	35
0.85	55
0.85	35
0.95	45

Table 3.7: 135° Model Test Matrix (Front Position, Spray Perspective)

Run	Frequency (Hz)	Span (%)	Run	Frequency (Hz)	Span (%)
1	0.80	50	26	0.80	40
2	0.95	35	27	0.80	50
3	1.00	45	28	0.80	55
4	1.00	55	29	0.80	55
5	1.00	45	30	0.80	35
6	0.90	45	31	0.95	50
7	0.85	50	32	0.95	55
8	0.80	45	33	0.90	50
9	1.00	35	34	0.85	45
10	0.85	50	35	0.80	35
11	0.85	40	36	0.85	40
12	0.80	45	37	0.90	50
13	1.00	40	38	0.95	40
14	1.00	40	39	0.90	35
15	0.85	45	40	0.95	50
16	0.95	55	41	0.90	35
17	0.85	55	42	0.85	55
18	0.90	55	43	0.90	40
19	1.00	50	44	0.95	35
20	0.85	35	45	1.00	35
21	0.95	40	46	0.85	35
22	0.90	45	47	1.00	55
23	0.90	45	48	0.95	40
24	0.95	40	49	1.00	50
25	0.80	40	50	0.95	45

Table 3.8: Refined Final Test Matrix

Chapter 4

Experimental Results

4.1 Introduction

This chapter documents the results of the experimental procedures and measurements detailed in Chapter 3. The primary method of presenting quantitative results is graphically through plots, however, supporting tabulated data is provided in the Appendix. The tabulated data represents mean values for replications of trial runs, as opposed to individual run results in an effort to stay concise. The second method of delivering results found is through an image based qualitative summary of spray event characteristics and behaviours. Additional background information concerning data analysis techniques and post processing is included in order to give sufficient contextual background in explaining how results were obtained and interpreted. Following, sections are broken up that summarize the results found from each model set up used. The results that are summarized are the impact pressures as a function of the dimensionless wave steepness, along with the wave heights and wavelengths that are associated with the impacts. The qualitative image analysis is conducted for the final model in the configuration of $\alpha = 0^\circ$ and $\beta = 135^\circ$. Finally, a brief comparison between the results found in this thesis and results found in the literature, both through prior experimentation and model development is presented.

4.2 Data Analysis and Post Processing Techniques

Each trial run conducted in the tow tank resulted in a LabVIEW log file for each measurement device that could be downloaded for later analysis. The log file formatting is in an NI LabVIEW TDMS (Technical Data Management Solution) format, but can be opened in Excel and then saved in the Excel XLSX format. Specific columns from the Excel data files could then be uploaded into Matlab for analysis and plotting purposes. Excel was then retained for bulk data management and organization, as well as performing simple calculations such as wavelength.

4.2.1 Pressure Sensors

The analysis of the pressure signal data for all trials was conducted in a similar manner, albeit with a subtle difference for the initial trials. The signals from the pressure sensors exhibited a noticeable amount of electrical noise during experimental trials. It was presumed through troubleshooting the sensor wiring that the source of the noise was most likely AC voltage entering the DC power supply. The difference in analysis previously mentioned was the method of conditioning the noisy pressure sensor signals. The noise was initially treated by using MATLAB signal conditioning of the data files for the tests using the flat plate model and the 120° model. The specific tool used was a Savitzky-Golay digital filter, which is a filter that uses polynomial fitting by linear least squares (MATLAB, 2016). The filter essentially over samples the recorded data to attempt to reduce the effects of the interfering noise and then smooths the result. When setting up the final tests for the 135° model, LabVIEW signal conditioning tools were discovered and subsequently used. A low pass filter can also be used to treat the

unwanted noise, and in this case a digital filter within LabVIEW was used (National Instruments, 2016). Unfortunately, some residual noise was still in the signals, which can be considered a source of measurement error. The error retained with the initial Savitzky-Golay filtering is approximately ±0.05 kPa, while the digital low pass filter in LabVIEW retained approximate ±0.11 kPa error due to noise.

Since the pressure of interest is due to an impact, the impact pressure can be thought of as a sort of relative pressure between a maximum and the ambient reading. The ambient pressure was first normalized to zero, using MATLAB, and the maximum value for the first significant impact was used as the impact pressure. Summarized results are located in the following plots with tabulated supporting data located in the Appendix.

4.2.2 Wave Probes

The Excel data files derived from LabVIEW TDMS log files were also used to analyse the wave probe data. The meaningful data directly extracted was wave height and wave period. Parameters subsequently calculated from the wave height and wave period were the wavelength and wave steepness.

MATLAB was again used for the datafile analyses. Wave height, H_w, was determined by subtracting the minimum water free surface elevation value (trough) from the maximum value (peak), giving the overall wave height for each wave probe in each configuration. The wave period, T_w, is a wave characteristic and represents the time it takes for a full cycle of the wave to elapse. In more practical terms the period can be defined as the distance between two signal peaks when plotted in the time domain.

A MATLAB peak finding function was used to isolate peaks and then subtract the spatial difference between the first two major peaks giving the wave period. The wavelength was then calculated once the period was known. The wavelength, L_w, of a travelling wave is defined by the following equation (Bhattacharyya, 1978):

$$L_w = \frac{gT_w^2}{2\pi} \tag{4.1}$$

where g is the acceleration due to gravity and T_w is the wave period. The wave steepness, k, is a non-dimensional representation of the steepness of a wave. It is defined by:

$$k = \frac{H_w}{L_w} \tag{4.2}$$

Finally, it is worth mentioning another attempted data analysis technique. The MATLAB Fast Fourier Transform function was used to transform the physical waveform into the frequency domain to isolate and report the dominant frequency. Originally, this was to confirm the frequency of the oncoming wave that originates from the wave board. It was, however, found that there was some error in the frequency calculations. It appears that since the data sampling rate (2-10 kHz) was so much higher than the wave frequencies ($\sim$1 Hz), that the resolution of the FFT output causes some inaccuracies and cannot be used.

4.2.3 Imaging

The primary purpose of understanding the wave impact pressures and wave characteristics is to provide a general basis and context for the occurrence of spray generation. High speed imaging was used for each trial and video was saved if appreciable spray

occurred, that is, if noticeable spray travelled into the camera field of view. The high speed imaging video files that were gathered can be provided for subsequent analysis and data collection by several different methods. First, the imagery can be analysed quantitatively through software packages such as NI LabVIEW and MATLAB to calculate spray droplet sizes and velocities. Due to a combination of the original thesis scope of providing large data sets for follow on research, the large volume of video (∼70 Gb), and the time it takes to analyse each video, a qualitative analysis of the spray generation will be provided here. Correlations and trends between wave steepness, impact pressure, and observed spray formation will be described below. Finally, still frames with a constant time step were collected for a series of trials for the most prominent spray occurrences and are shown in Figures 4.16 - 4.22.

4.3 Flat Plate

The first test runs were conducted using the flat model for reasons specified above, largely for its frontal surface area inducing spray the easiest. Initial exploratory trials were conducted to establish a rough baseline for the upper and lower bounds for the wave board frequency and span settings to induce spray. Trials were conducted so that video could observe both the sheet breakup and spray trajectories. The results for the measured impact pressures are plotted against the wave steepness for each scenario and are located below. The pressure measurements taken during the first day of tests had to be excluded due to inputting improper settings in the data acquisition settings.

The mean values for the wave impact pressure on the flat plate model with the side

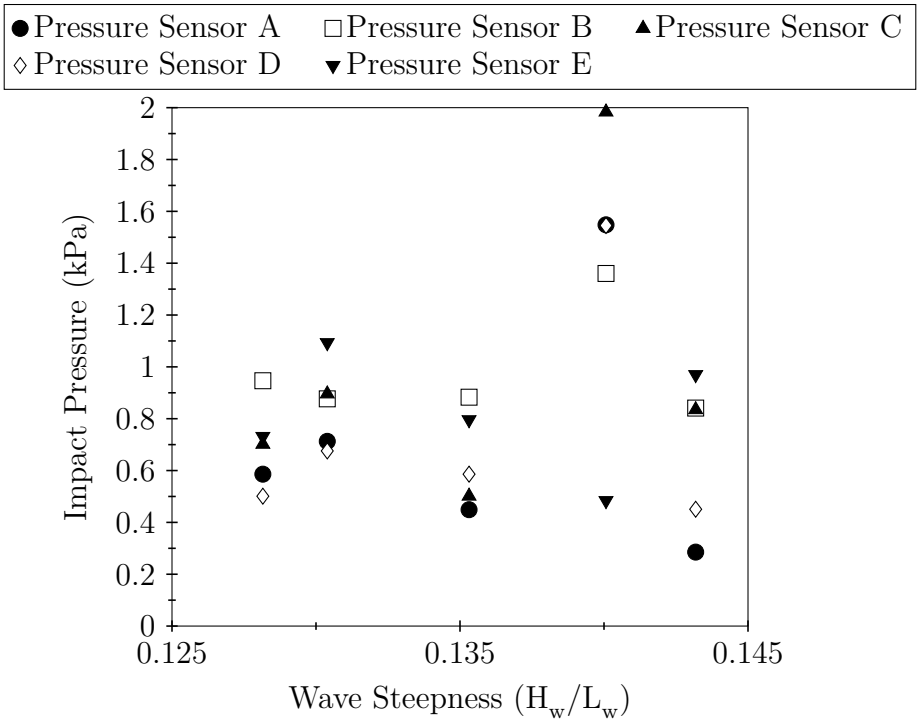

Figure 4.1: Flat Plate Model Impact Pressure (Side Position, Spray View)

position and spray perspective are plotted against the wave steepness k in Figure 4.1. The highest impact pressures peaked at around 1.4 - 1.6 kPa, with one outlier at approximately 2 kPa. The lowest impact pressure was approximately 0.2 kPa. It can be seen relatively easily that the data points exhibit quite a bit of scatter in the plot. However, even with the scatter, some general observations can be made. The lowest impact pressures tend to generally be focused around Pressure Sensors A and D while the higher pressures affect Pressure Sensors B, C, and E. What this means is that higher impact pressures occur on lower positions on the model. This tends to make intuitive sense, because more of the wave's energy would contribute to the impact. A possible cause for the scatter and overlapping data points could be the physical distance between the sensors. The diagram shown in Figure 3.5 of the pressure sensor placement illustrates the difference in sensor proximity for each

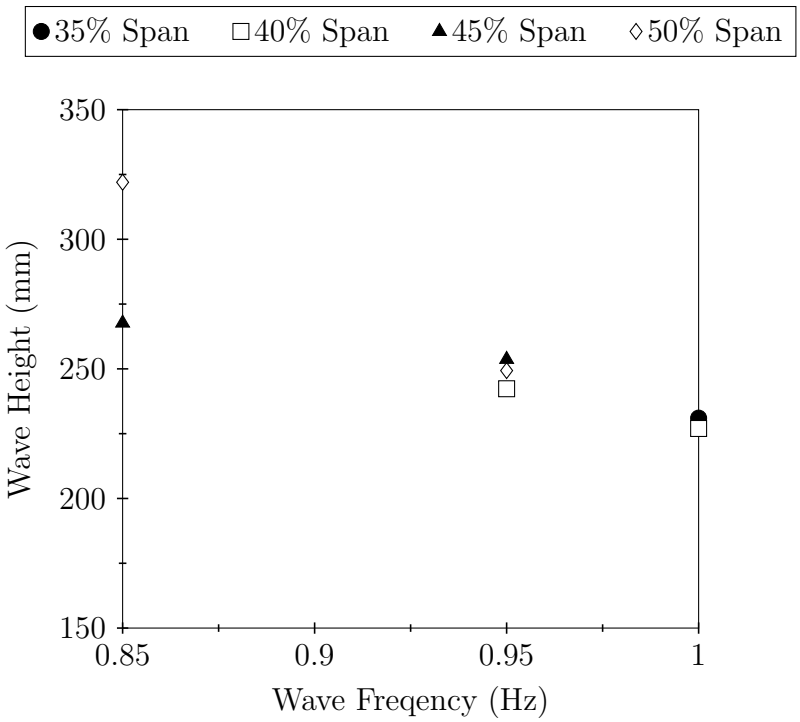

Figure 4.2: Flat Plate Model Wave Height (Side Position, Spray Perspective)

model configuration. The intent was to have the sensors arranged in an array of two columns, side by side. The left column had three sensors, separated by a distance of approximately 2.25 inches vertically and the right column had two sensors positioned at roughly the midpoints between sensors on the left column. Placing sensors farther apart in the vertical direction seemingly alleviated this issue, as seen in the final tests of the model ($\alpha = 0°$; $\beta = 135°$) where sensors were 6 inches apart vertically. The effect of the pressure sensor placement can be understood when thinking in terms of the overall height of the impacting waves. The measured impact pressures of three sensors placed closely together in relation to the height of the wave would not show much measurable difference in pressures. The contrast would be sensors placed across the full height distribution of the wave that would measure more of a widely varied pressure distribution.

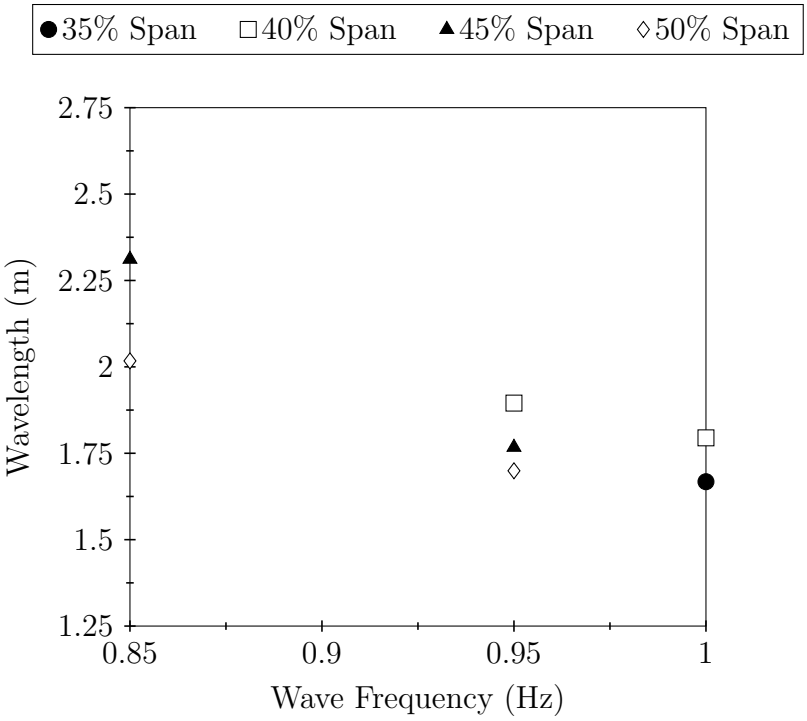

Figure 4.3: Flat Plate Model Wavelength (Side Position, Spray Perspective)

Plots illustrating the characteristics of the wave steepness components are shown in Figure 4.2 (wave height) and 4.3 (wavelength). Figure 4.2 plots the weight hight for wave probe 2 as a function of wave maker frequency for separate span settings. This is the wave probe that is in line with the model face, and therefore a representation of the wave height associated with the impact. The results reveal a trend that correlates a decreasing wave height with an increasing wave maker frequency. It also appears that for a given frequency, wave height increases with decreasing span. The plot for the wavelength (Figure 4.3) also shows a relationship between the applied wave board frequency and wavelength. The wavelength tends to decrease with an increasing frequency and larger span. This tends to make sense because $L_w \sim T_w^2$ and $T_w \sim 1/f$, by definition.

Plots for the second full set of collected data for the flat plate model are Figures

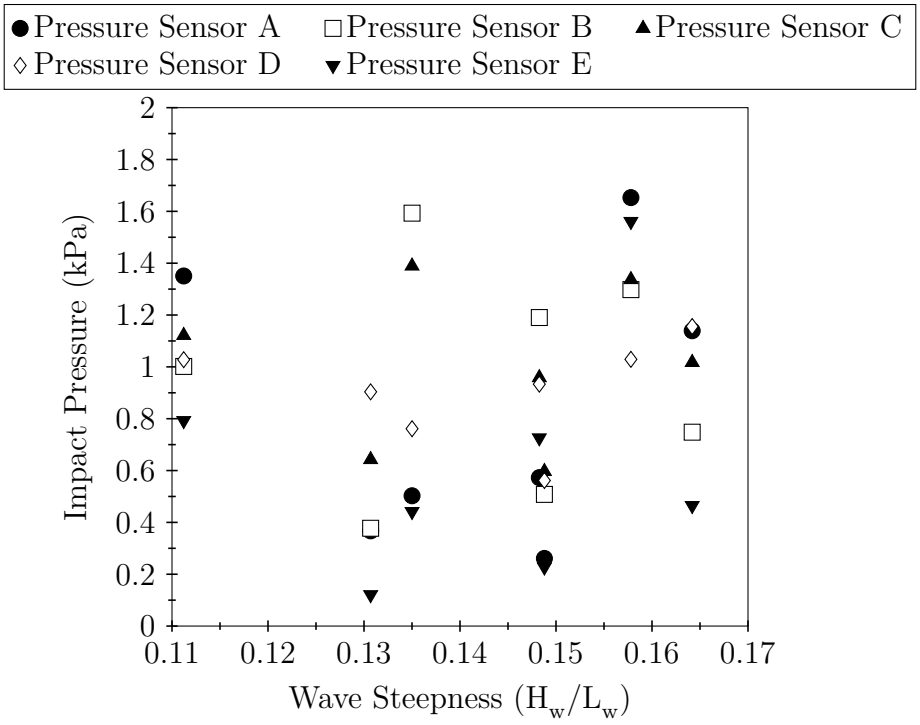

Figure 4.4: Flat Plate Model Impact Pressure (Front Position, Sheet Perspective)

4.4 - 4.6 below. The model is oriented physically in the same manner as previously, but the camera positioning is different. The camera for this set of experiments was located in the front position, focusing on the sheet breakup perspective. Unfortunately, inconsistent results for the impact pressure continued in this test. The lowest impact pressures were around approximately 0.2 kPa while the maximums were about 1.6 kPa. The scatter here could still be attributed to the close positioning of the pressure sensors. Also, having prior knowledge of an appropriate range of frequencies and spans would enable more effective iterative testing, and provide higher quality results. The wave heights for each wave probe continued to exhibit similar trends.

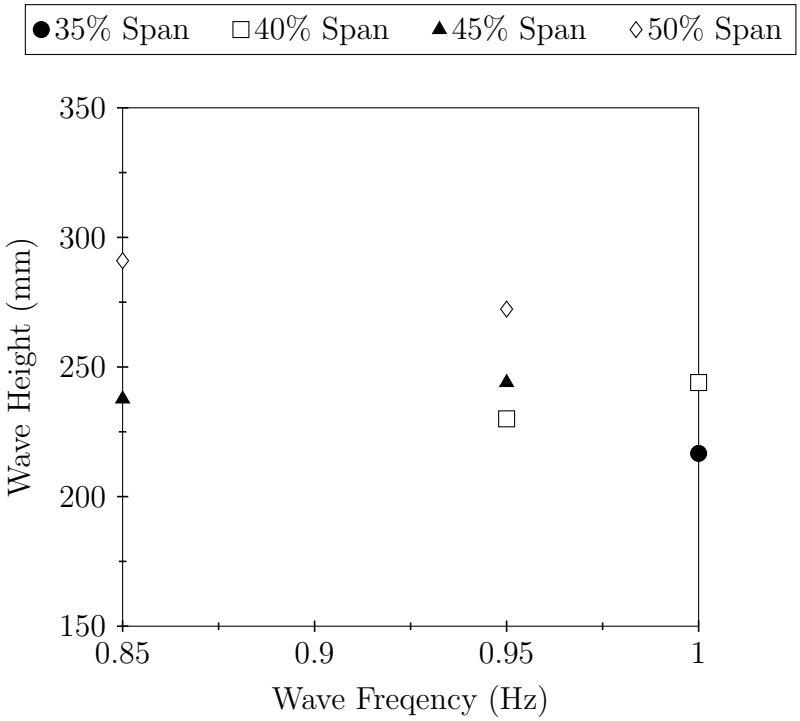

Figure 4.5: Flat Plate Model Wave Height (Front Position, Sheet Perspective)

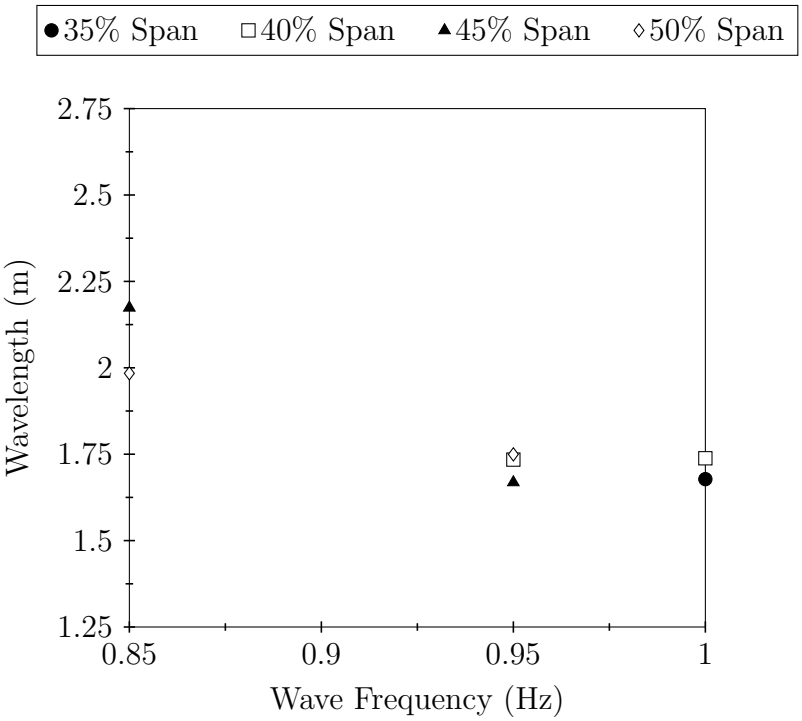

Figure 4.6: Flat Plate Model Wavelength (Front Position, Sheet Perspective)

4.4 120° Angle Model

The second model to be used was designed during the testing of the first model, and finally fabricated by Technical Services after testing was completed. The same measurements were taken, however unforeseen issues occurred that were not discovered until the data analysis began. The measurements obtained from the pressure sensors were erratic and do not appear to be valid results. The same test procedure was conducted and the same conditions were met as for the flat plate model, so the cause of these erratic measurements is unknown. Possible causes could stem from an electrical or circuity error, or the physical mounting of the sensors to the model having issues. It was confirmed that data was being acquired through the DAQ at the time of testing, but the quality and extent of error was not fully known until the later data processing.

The data from the wave probes was processed and had consistent results. The plots of these results were included in the previous section to provide context and relations to the measured impact pressure data. Consequently, they will not be included here due to the insufficient pressure plot to relate to. However, the tabulated averages for the results of the wave probes are located in the Appendix.

The high speed camera captured video of spray effects that differed from those observed with the first flat plate model. This can be expected due to the smaller frontal surface area, and as a result, fewer instances of induced spray occurred. The spray formation continued to largely be ejected vertically upon impact, but the water sheet breakup behaviour was different. Previously, the water sheet formed upward and tended to break up into droplets. The water sheet travelled along the sides of the model in a swell-like fashion at times if the wave was big enough.

4.5 135° Angle Model

The pressure sensors were recalibrated and checked for functionality prior to use with the final model. Sensor linearity and calibration agreement was very similar to the prior checks when sensors were fully functional. The erratic behaviours and malfunctions from the previous set up are therefore still unknown. The highest quality results obtained were with the final model ($\alpha = 0°$; $\beta = 135°$), which coincided with designing the experiment through the Design Expert 9 software package. These tests deliberately tested within set ranges of wave board frequencies and spans, at even intervals. The range of wave board frequencies and spans was chosen based off of the previous results and observing which combinations were most appropriate for spray testing. The range of parameters tested were 0.85 - 1.0 Hz and 35 - 55% span, in 5 Hz and percent span increments. Not unsurprisingly, the quality of the data results and plots are much higher than previously assessed. The vertical spacing of the sensors also assured higher quality test results.

The immediate observation is the obvious trend in the impact pressure as a function of wave steepness during the camera side position trial, with $\alpha = 0°$. The impact pressure increases linearly as the wave steepness increases. A table detailing the equations for the best fit lines and their corresponding coefficients of determination (R^2) for the impact pressures in Figure 4.7 is below. Furthermore, the magnitude of impact pressure is smallest with the lowest positioned sensor, and highest with the top placed sensor. These results make sense from an intuitive standpoint. Best fit lines are fitted to the plot below (Figure 4.7). The fit is best for this model, with a mean slope of 9.362. Therefore, the impact pressure can be seen as roughly proportional to the wave steepness by a factor of 9.362. The impact pressure for Sensor A ranged from 1.08

- 1.70 kPa, Sensor C ranged from 0.53 - 1.22 kPa (with one 1.33 kPa outlier), and Sensor B ranged from 0.10 - 0.86 kPa. It can be seen that higher occurrences and magnitudes of spray occurred during conditions of higher wave steepness and height, and consequently higher impact pressures.

Pressure Sensor	Correlation Equation	(R^2)
A	P = 8.9645k + 0.3058	0.4997
B	P = 8.5926k - 0.7505	0.5665
C	P = 10.529k - 0.4349	0.4465

Table 4.1: Impact Pressure Correlations for 135° Model (Side Perspective)

The wave heights continued to exhibit a relationship to the set wave board frequency, with decreasing wave heights for increasing frequencies. The wave heights ranged from a maximum of approximately 160 - 350 mm. Finally, the wavelengths ranged from approximately 1.50 - 2.47 m.

This model was then reconfigured to vary with the vertical axis, setting $\alpha = 20°$. At this point the camera was still in the side position. The impact pressure measurements demonstrated trends as before, but they were a little more scatted than previously observed, along with some overlap. Best fit lines are again fitted, but the fit was not as good as before. Tabulated values for the correlation equations are also located below. The main cause of this scatter is likely the angle of the pressure sensor face with respect to the in coming water. Previously, the sensor faces were orthogonal to the water surface, instead of being tilted. The impact pressure for Sensor A ranged from 1.09 - 2.05 kPa, Sensor C ranged from 0.44 - 2.05 kPa , and Sensor B ranged from 0.11 - 1.32 kPa (with one 2.85 kPa outlier). Wave heights for these impacts also ranged from 157 mm to 323 mm, and the wavelengths varied from 1.31 - 2.66 m. A noticeable difference in the spray formation occurred with this model configuration.

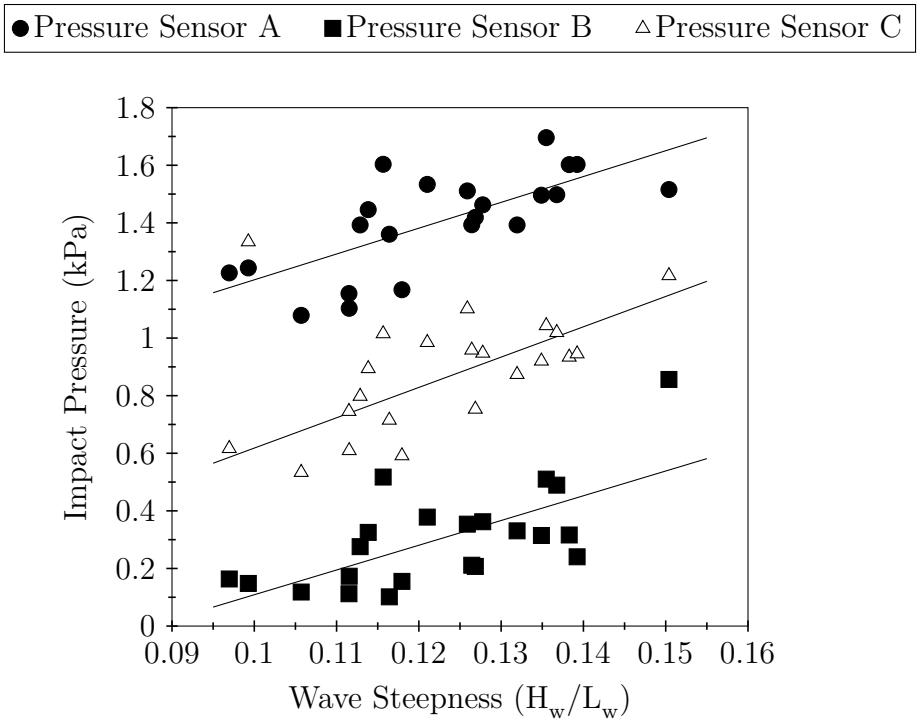

Figure 4.7: 135° Model Impact Pressure (Side Perspective)

The spray tended to deflect rearward and upward upon impact due to the model being tilted forward. Furthermore, the forward tilt seemed to lower the likelihood of spray formation compared to the flat faced models.

Pressure Sensor	Correlation Equation	(R^2)
A	P = 3.413k + 1.0317	0.0390
B	P = 10.183k - 0.8038	0.2257
C	P = 4.6572k + 0.5524	0.0304

Table 4.2: Impact Pressure Correlations for 135° Model (Side Position, $\alpha = 20°$)

The final trial retained the model's previous geometric set-up, but the camera position was changed to the front. The initial plan was to replicate the same number of trials in accordance with the designed test plan, but unforeseen time limitations in the lab precluded this. The alternate course of action was to pick several of the best performing frequency and span combinations tested previously and continue as normal.

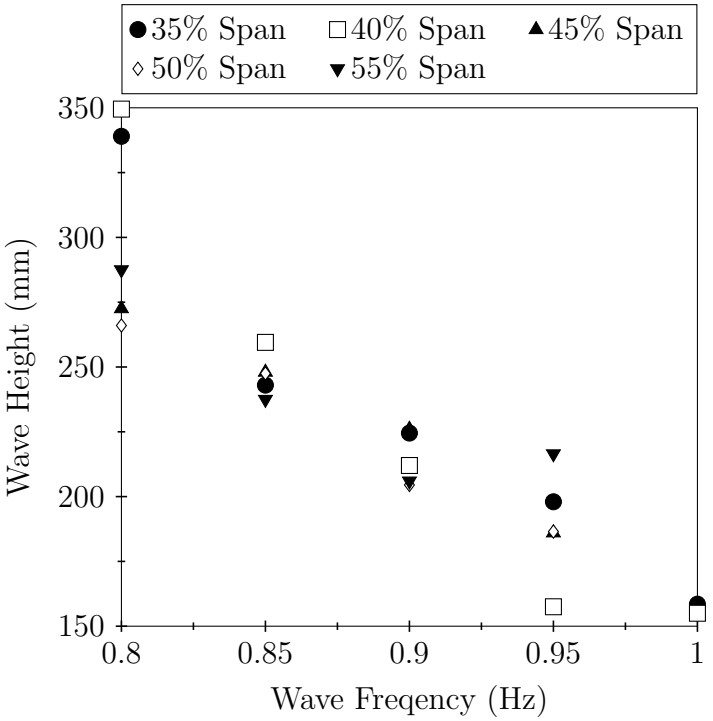

Figure 4.8: 135° Model Wave Height (Side Position)

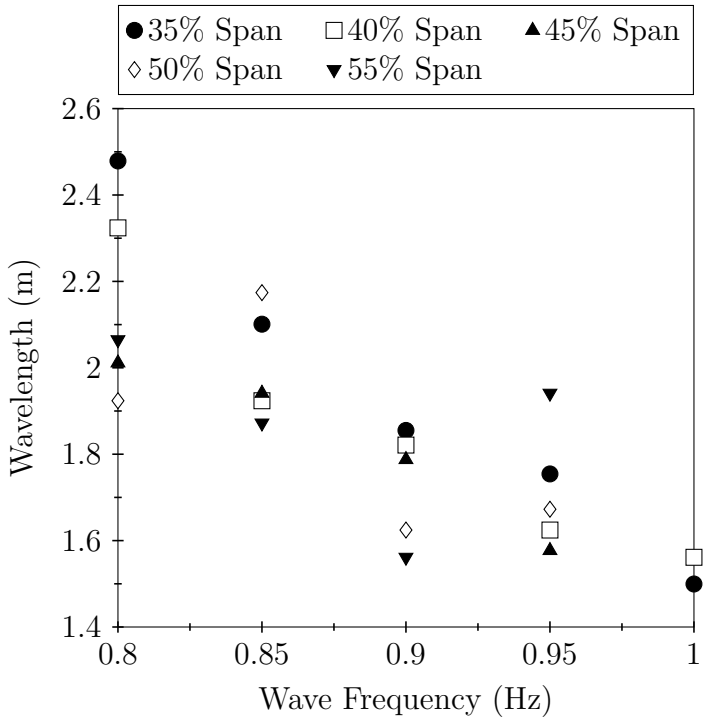

Figure 4.9: 135° Model Wavelength (Side Position)

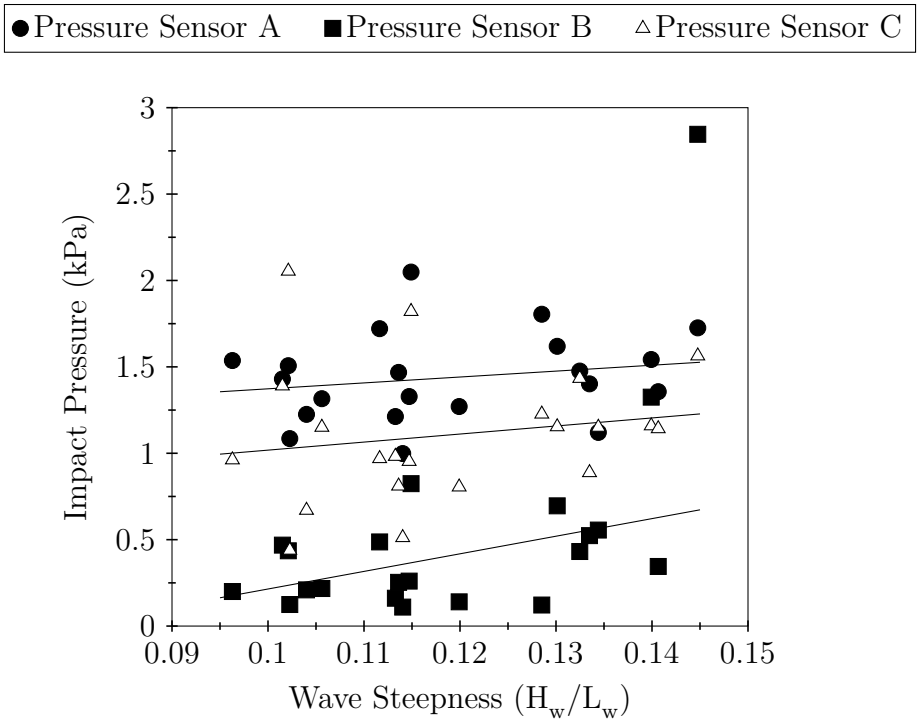

Figure 4.10: 135^o Model Impact Pressure (Side Position, $\alpha = 20°$)

Nine combinations were chosen for the front view tests. The trend for the increasing impact pressure with increasing wave steepness continued, and trend lines are again fitted to the plot in Figure 4.13 and tabulated below. This configuration resulted in Sensor A ranging from 1.06 - 1.71 kPa, Sensor C ranging from 0.62 - 1.37 kPa, and Sensor B ranging from 0.14 - 0.74 kPa. Wave heights for these impacts also continued the same trend as before, ranging from 181 mm to 315 mm, and with wavelengths varying from 1.56 - 2.29 m.

Pressure Sensor	Correlation Equation	R^2
A	P = 3.7887k + 0.965	0.2956
B	P = 5.7401k - 0.2941	0.7546
C	P = 3.6068k + 0.6563	0.2853

Table 4.3: Impact Pressure Correlations for 135° Model (Front Position, $\alpha = 20°$)

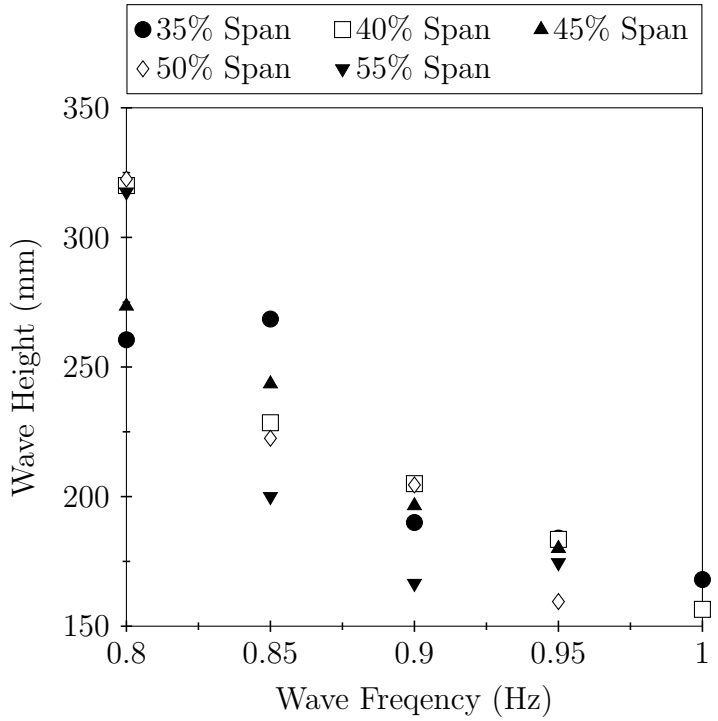

Figure 4.11: 135° Model Wave Height (Side Position, $\alpha = 20°$)

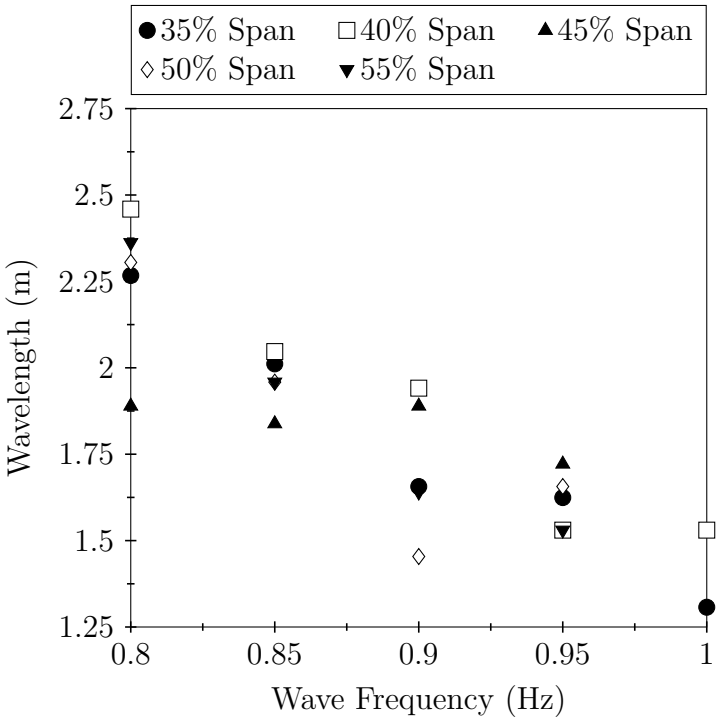

Figure 4.12: 135° Model Wavelength (Side Position, $\alpha = 20°$)

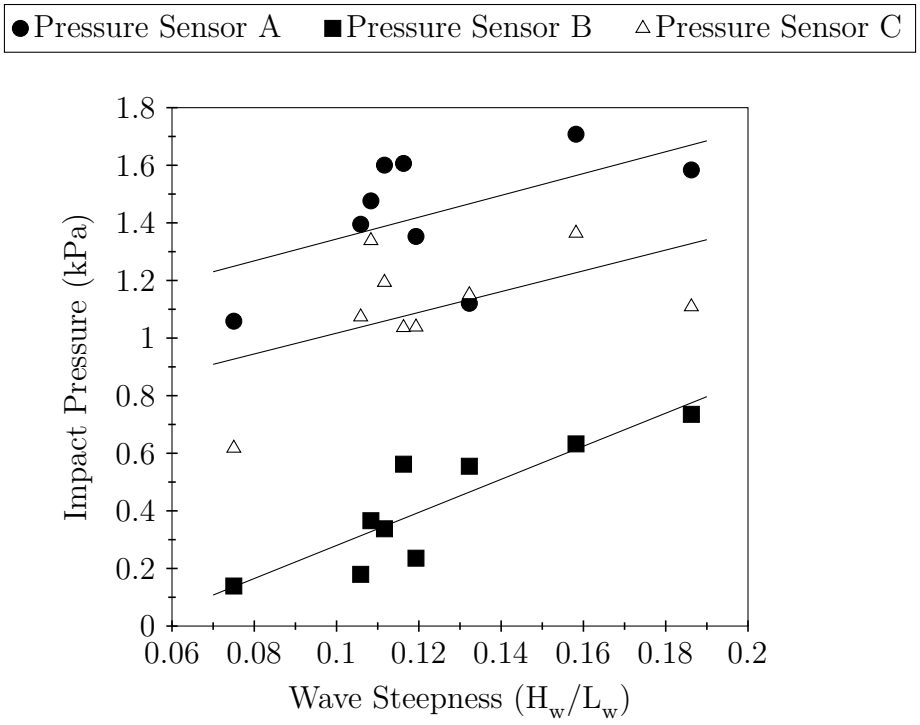

Figure 4.13: 135° Model Impact Pressure (Front Position, $\alpha = 20°$)

4.6 Image Analysis

This section serves as a discussion of the qualitative analysis of the spray formation observed during the course of the experimental trials. Qualitative analysis can serve as a valuable method to understand trends and behaviours in physical processes.

High speed imaging was acquired for all model configurations in the positions and perspectives as detailed above. The final model ($\alpha = 0°$; $\beta = 135°$) provided the most favourable results in terms of pressure sensor measurements and had experimental trials designed and conducted in the most thorough manner. Therefore, the image analysis here will focus on these results and trends. There were a total of 44 trials conducted for this configuration, with 22 of these being independent pairs. That is,

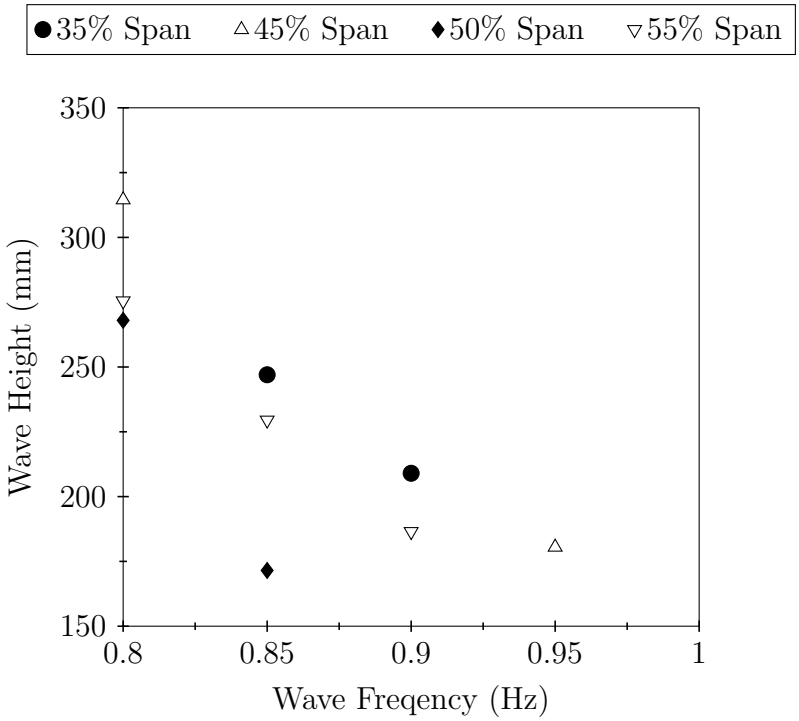

Figure 4.14: 135° Model Wave Height (Front Position, $\alpha = 20°$)

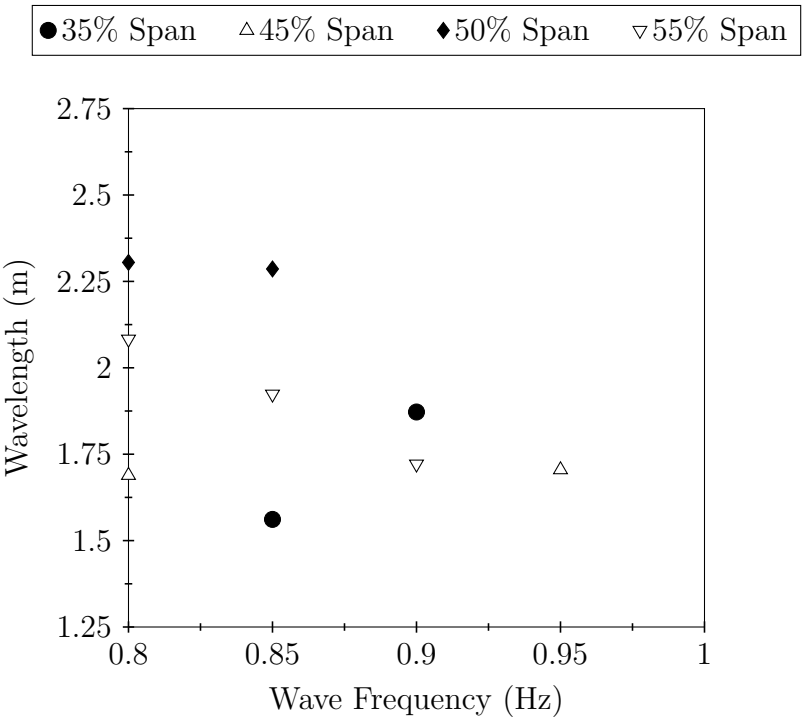

Figure 4.15: 135° Model Wavelength (Front Position, $\alpha = 20°$)

there were 22 pairs of wave board frequency and span pairs that were repeated twice. Ideally more repetitions would have been conducted, but again, time was a limiting constraint. The following collection of spray image series shows the initial evolution of spray upon wave impact to the droplets' higher elevations. Each series contains eight images with a step time of 0.5 s. The initial time t = 0 s was chosen as the moment right before spray became visible in the field of view. The model in the image has the configuration previously stated and the high speed camera recorded at 1000 fps. An interesting trend was observed following the correlations shown in Figure 4.7 (the relation between impact pressure and wave steepness).

The method of choosing which image series to present is based largely from the observed results obtained in Figure 4.7. It can be seen from this figure that as the wave steepness increases, the impact pressure trends upwards. Best fit lines show the upward trend has a slope of 9.362. The averaged impact pressures for Sensor A, shown in Figure 4.7, were sorted from highest to lowest. The largest ten measurements were chosen as a representative sample out of the total 22. The impact pressures range from 1.463-1.696 kPa, and the wave steepness within that set ranges from 0.116-0.150. This sample was then resorted in terms of highest to lowest wave steepness. It was found that seven of the top ten wave steepness values are also within the top ten impact pressure values. The image collections below are listed in order of descending wave steepness. Some features of their spray characteristics will be outlined below.

Several interesting characteristics of the spray formation were observed in the imaging data. The most notable were the largest spray events largely coinciding with higher wave steepness (and consequently wave height), which was in turn correlated to higher magnitudes of impact pressure. This correlation was made largely by personal observation after many trials, and by recognizing that the video files for the largest

spray events also generally coincided with the maximum impact pressures. This observation makes sense from an intuitive stand point. Larger wave heights contain more liquid water mass and impose more energy onto an object upon collision, with larger amounts of spray being generated as a result of the energy dissipation. Several empirical observations were also made during the experimental trials that support these finding. It was found that waves generated from wave maker settings ranging from roughly 80 - 85 Hz and 40 - 45% span generally created spray the most.

Another characteristic that is worth mentioning is type of behaviour observed during these spray events. There can be seen roughly two categorical behaviours of the spray. One set can be seen when a wave impacts and its water sheet follows the model's side contour while ejecting droplets. Figures 4.2, 4.4, and 4.7 demonstrate this trend most clearly. The other main behaviour is when spray is ejected almost immediately upon impact, and no significant water sheet is formed. This can be seen in Figure 4.3 and 4.8.

(a) t=0.00 s

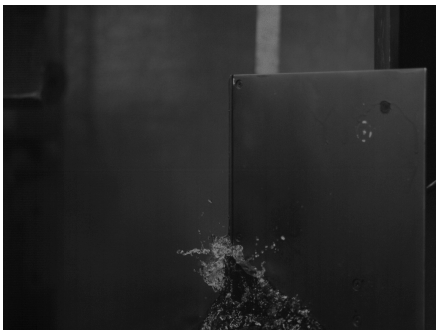

(b) t=0.05 s

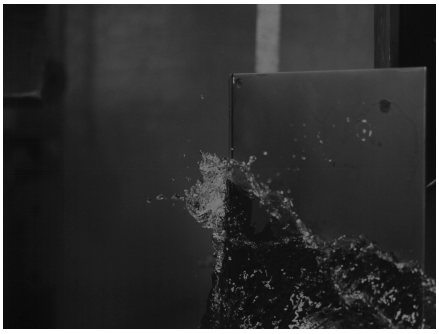

(c) t=0.10 s

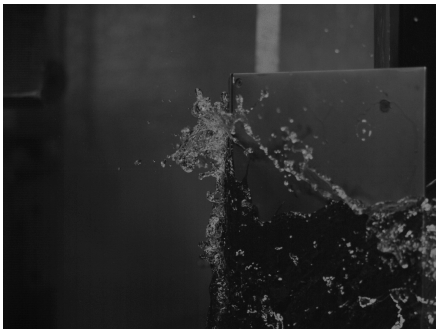

(d) t=0.15 s

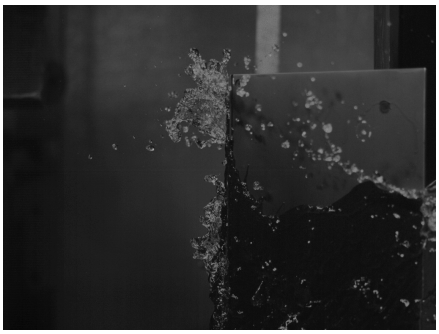

(e) t=0.20 s

(f) t=0.25 s

(g) t=0.30 s

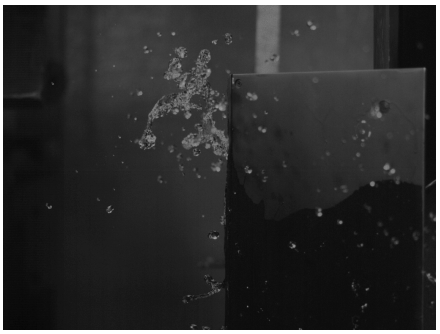

(h) t=0.35 s

Figure 4.16: 0.80 Hz, 40% Span (k = 0.150)

(a) t=0.00 s

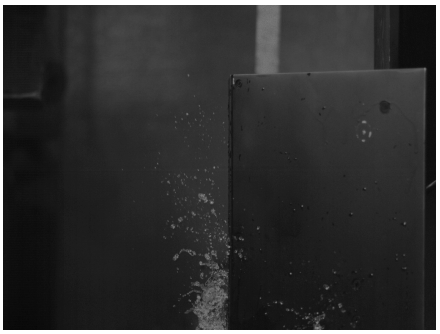

(b) t=0.05 s

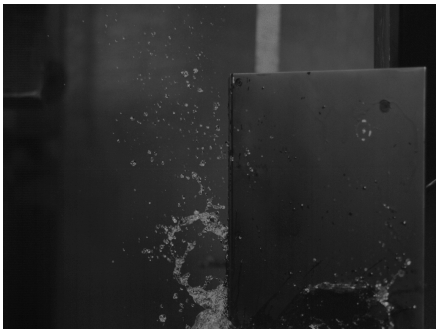

(c) t=0.10 s

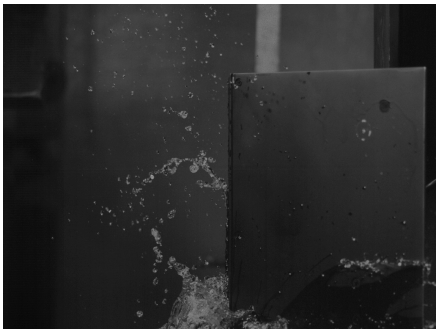

(d) t=0.15 s

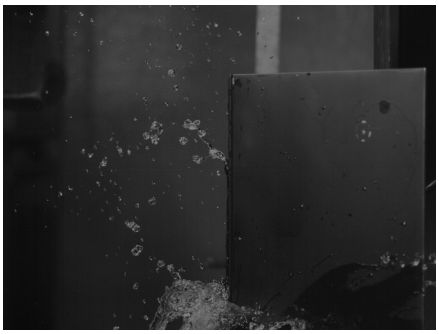

(e) t=0.20 s

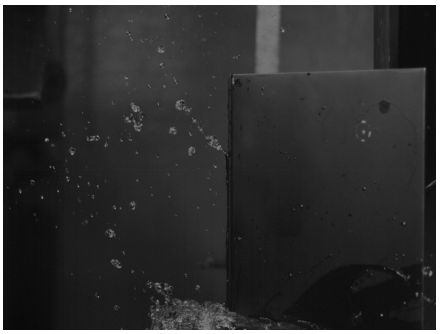

(f) t=0.25 s

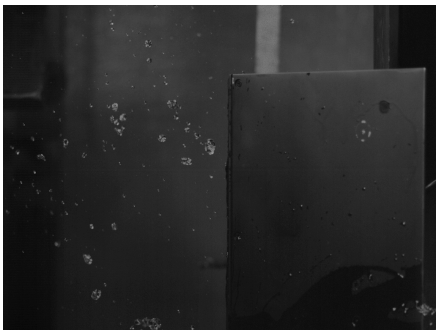

(g) t=0.30 s

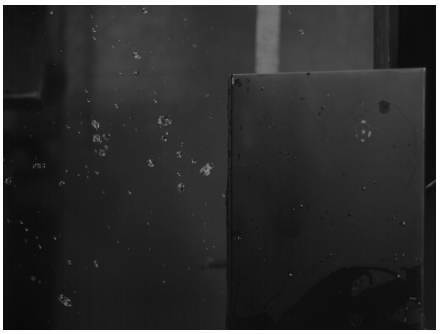

(h) t=0.35 s

Figure 4.17: 0.80 Hz, 55% Span (k = 0.139)

(a) t=0.00 s

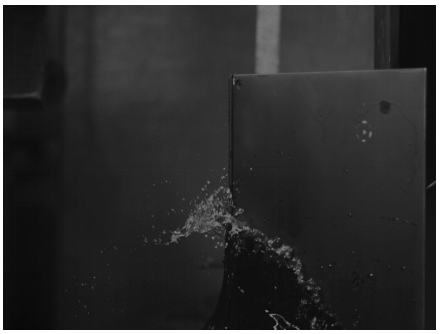

(b) t=0.05 s

(c) t=0.10 s

(d) t=0.15 s

(e) t=0.20 s

(f) t=0.25 s

(g) t=0.30 s

(h) t=0.35 s

Figure 4.18: 0.80 Hz, 50% Span (k = 0.138)

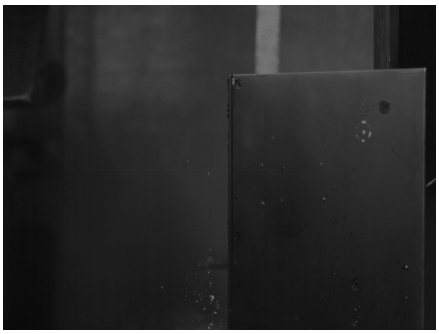

(a) t=0.00 s

(b) t=0.05 s

(c) t=0.10 s

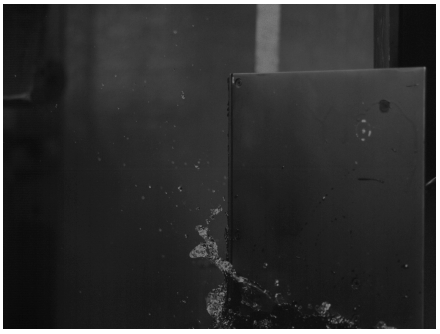

(d) t=0.15 s

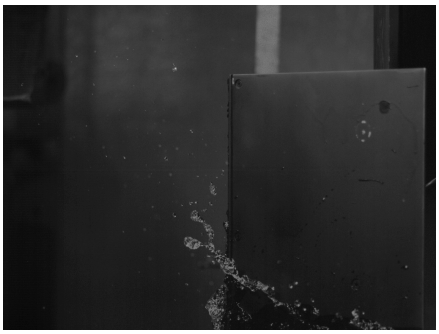

(e) t=0.20 s

(f) t=0.25 s

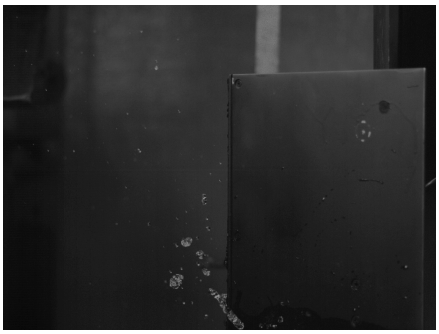

(g) t=0.30 s

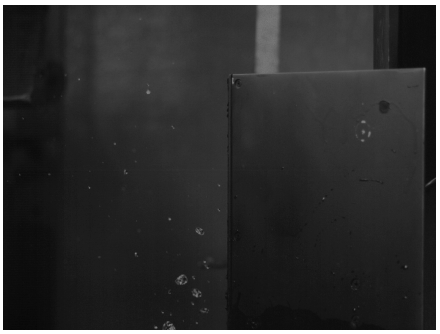

(h) t=0.35 s

Figure 4.19: 0.80 Hz, 35% Span (k = 0.137)

(a) t=0.00 s

(b) t=0.05 s

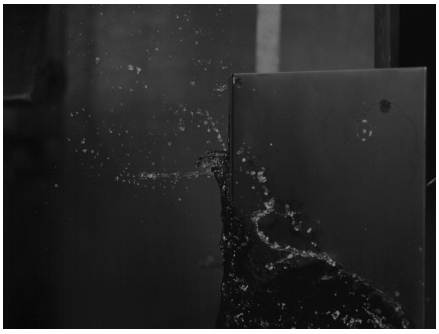

(c) t=0.10 s

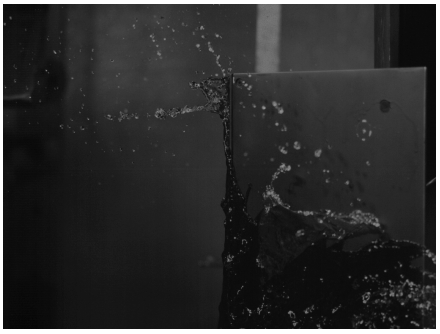

(d) t=0.15 s

(e) t=0.20 s

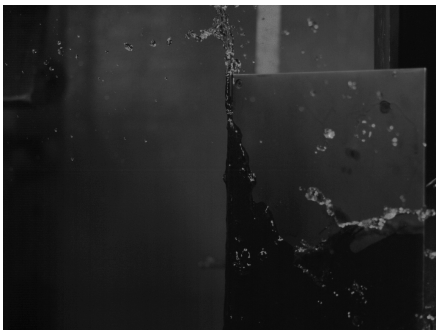

(f) t=0.25 s

(g) t=0.30 s

(h) t=0.35 s

Figure 4.20: 0.80 Hz, 45% Span (k = 0.135)

(a) t=0.00 s

(b) t=0.05 s

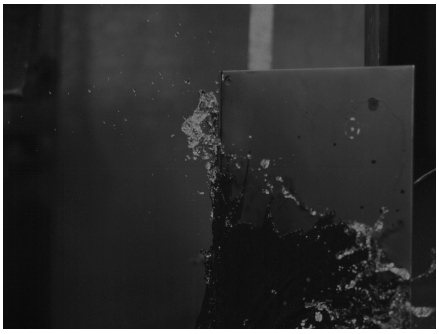

(c) t=0.10 s

(d) t=0.15 s

(e) t=0.20 s

(f) t=0.25 s

(g) t=0.30 s

(h) t=0.35 s

Figure 4.21: 0.85 Hz, 40% Span (k = 0.315)

(a) t=0.00 s

(b) t=0.05 s

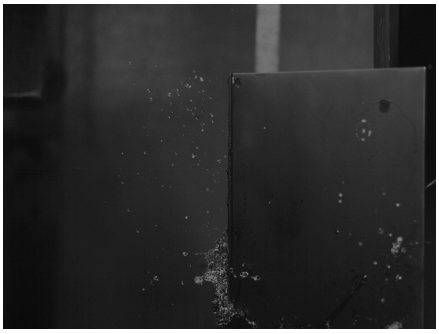

(c) t=0.10 s

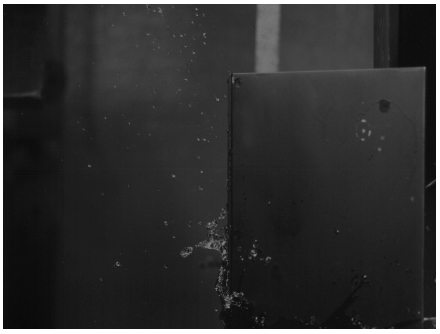

(d) t=0.15 s

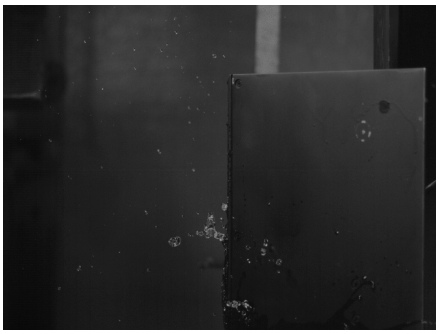

(e) t=0.20 s

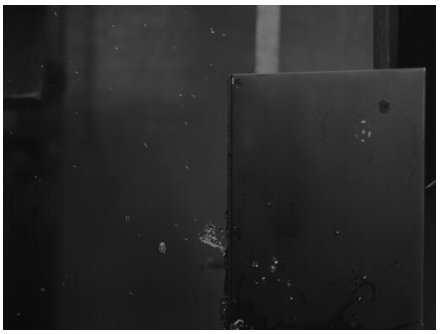

(f) t=0.25 s

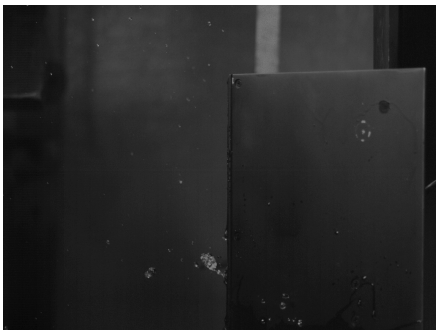

(g) t=0.30 s

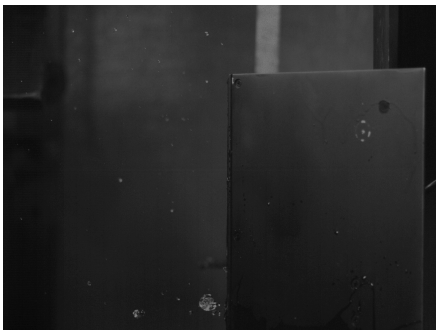

(h) t=0.35 s

Figure 4.22: 0.85 Hz, 45% Span (k = 0.128)

4.7 Comparison to Published Results and Models

This section aims to provide a brief comparison of the results gathered in this project to previously published results and models in the literature. The primary sources of comparison for the pressure data gathered are published wave impact and spray experiments, while wave spray models are used as a comparison for the spray video data.

The impact pressure measurements during the trial runs of the final model ($\alpha = 0°$; $\beta = 135°$) serve best as a basis for comparison. This is due to the highest quality of results obtained. Highest quality in this instance means that the data points were acquired with the most observable physical trends. The highest impact pressures ranging from roughly 1.08 to 1.70 kPa agree with the behaviours reported by Fullerton et al. (2010). The impact pressures from the other model configuration ($\alpha = 20°$; $\beta = 135°$) also fall in line with the general order of magnitude of this previous study. Furthermore, the recorded shape of the time evolution of the impact pressures visually look similar to the ones conducted by Fullerton et al. (2010) and Greco et al. (2012). This study by Fullerton et al. (2010)was conducted by a researcher at a US Navy research centre, and reported experimental impact pressures of approximately 0.75 - 1.5 kPa for lab scale experiments with similar non breaking wave characteristics. The test object for this study was a rectangular blunt object placed into the water surface at varying depths and angular orientations. One other study concluded reached conclusions of greater impact studies. Impact pressures ranging from roughly 2 - 6 kPa were observed by Greco et al. (2012), although this was with a larger wave steepness of 0.2. This study investigated wave slamming on the bows of ships and the subsequent water shipment across the decks. This study was somewhat different in

that the pressure measurements were mostly on the side of the bow, in relation to the oncoming waves. Nevertheless, the results are valuable to this this. The results and lessons learned from both of these previous studies provide important conclusions. Most importantly, they serve as a validation in the impact pressure measurement technique employed for this thesis, because of the similar magnitude of laboratory measurements taken as well as the general trend in the time evolution of the individual impact measurements.

A final qualitative comparison and observation can be made to the previous models described in Chapter 2. These relate to the findings in the project of increased impact pressure trending with increased wave steepness, and how higher instances of wave spray are inter-related. The equations predicting collision generated spray flux (Equations 2.4 - 2.9) are mostly all primarily driven by the colliding wave height, and the work by Chung et al. (1998) developed upon this by developing relations in the lab scale to correlate spray flux to ship speed and wave height. The results from this thesis project can be used in several useful manners. The correlating equations presented in Tables 4.1 - 4.3 could be used in a predictive manner along with equations similar to the ones previously discussed in Chung et al. (1998). A future study, using the technique developed in this thesis, could study spray fluxes in the lab scale along with their respective impact pressures. The potential for more robust studies is compounded even more strongly with the introduction of high speed imaging, such as in this thesis. Image processing and studying high speed imaging would serve as an important compliment to cylindrical spray flux collectors by understanding the trajectory and behaviours more in depth. All of these developments, observations, and results can paint a picture from a qualitative stand point, where at the most basic level the larger waves tend to create more instances of spray events, which in

turn correlate to higher impact pressures. The results both measured and observed through video offer valuable insights into understanding spray formation behaviours at the lab scale as well as serve as a valuable piece of validation work for follow on computational models. This can be seen especially by the agreement and technique validation seen when compared to previously published studies.

Chapter 5

Conclusions and Recommendations

The intent of this thesis project was to create a laboratory scale test set-up and conduct experimental trials examining collision generated spray. This was in conjunction with the overall effort of the Marine Icing research group at Memorial University, whose aim is to further the understanding of marine icing processes.

Section 5.1 discusses conclusions drawn from the experimental trials, trends and correlations observed, and lessons learned throughout the course of the thesis. Section 5.2 then discusses specific recommendations pertinent to the works completed as well as some overall recommendations for future research.

5.1 Conclusions

The first model to be utilised for the spray generation testing in the tow tank was the flat plate model. Measurements of impact pressure and wave characteristics were taken along with high speed imaging of the spray formation. The intent of the pressure sensor measurements was to both provide validation data for future research and to also provide a greater understanding of the conditions in which spray forms in the laboratory setting. The results of the pressure sensor measurements unfortunately

demonstrated some scatter in the data points. This could possibly be attributed to two main causes. First, the vertical positioning of the sensors was probably too close together. The narrow spacing seemed to be not quite enough space to resolve the impact pressure variation of the impacting waves, causing some overlap and similar readings. Another cause of the scatter was probably caused by the test method itself. Since the test matrix range of values had not been fully refined, there was not a full and completely iterative range of values tested. Therefore, higher quality results would have probably been achieved if sensors were placed farther apart, along with a more complete range of iterated test parameters chosen. The observable results from the imaging confirmed that choosing a flat plate was a good start in generating spray. The range of wave board settings (and therefore wave properties) that experienced higher occurrences of spray generation were typically around 80-85 Hz. The spray formation tended to also either develop immediately upon impact, or develop from the breakup of liquid water sheets.

After testing with the flat plate model was completed, a second model was introduced. This model contained variable angle characteristics as defined in Chapter 3, and was set to $\alpha = 0°$ and $\beta = 120°$. Imaging positions and methods were similar to what was used for the flat plate model. Similar wave board settings were set during the tests, and the same impact pressure and wave characteristics measurements were made. It was not discovered until after testing was completed and the data was being analysed that the pressure sensors recorded faulty data. Possible causes could stem from incorrectly wiring the sensors some error in the data acquisition. This makes it difficult to qualify the occurrences of spray generation, and poses a problem with the aim of gathering validation data. A noticeable, yet predictable change in spray characteristics occurred, namely, the lower occurrence of spray due to a narrower

frontal surface area.

The experimental trials of the final model configuration ($\alpha = 0°, 20°$; $\beta = 135°$) produced the highest quality results that can be quantified and qualified in several different ways. This can likely be attributed to systematically varying the test parameters of wave board and span across five values each. First, and most apparent, were the impact pressure measurements. Trends can be seen between the non-dimensional wave steepness and the impact pressure for all sensors. Furthermore, it is clear that the impact pressure increases with decreasing sensor position elevation, which makes intuitive sense. Linear fitted lines were then calculated and fitted to the plots, where the average slope is 9.362. The two plots of the dependent parameters of the wave steepness, wave height and wavelength, also show clear trends. The correlation between impact pressure and wave steepness was then considered in the context of the imaging of the spray generation. It can be seen that generally as wave steepness, and therefore impact pressure, increases, the instances of noticeable spray generation occur. Seven of the highest ten instances of wave steepness coincided with saved imagery files for the best spray formation video. These were then qualitatively summarized and shown in images of their temporal evolution. The imaging revealed several trends in the spray formation. One such trend was for the colliding wave to immediately turn into ejecting spray, while another trend was that the liquid sheet would continue past the model before ejecting spray upward. The case of the colliding wave impacting and immediately ejecting spray can be observed in several cases of lower wave steepness. More steep waves tended to collide and then glide along the outer edge of the model before turning into spray. These trends can be briefly seen in Figures 4.16 - 4.22. It should also be noted that in some cases the collision of very large, very steep waves caused a violent impact, which in turn created an immediate

ejection of spray. More investigation of this behaviour is recommended.

An interesting behaviour in the wave heights can be made. It could be seen, such as in Figure 4.2, that the wave height does not vary that much as the wave board span varies. This was observed in several other cases with large wave board frequencies. This could be possibly be attributed to reaching the maximum limits in the wave maker capacity, due to the large energies related to such high frequencies. This could be further supported by observing that generally at the point of measurement, the waves were not limited by a breaking limit.

5.2 Recommendations

There are several recommendations that can be made that would improve the experimental tests conducted in the course of this thesis project. Other recommendations can also be made that could contribute to follow on research and continued investigations.

The measurements of the impact pressures agree with the general magnitude and behaviours of several previously published results using similar conditions (Fullerton et al., 2010; Greco et al., 2012). The most conclusive impact pressure measurements were made with the final model configuration. The noticeable difference with this model compared to the initial flat plate model was the pressure sensor placement, which had sensors placed 6 inches apart as opposed to 2.25 inches. This spacing contributed to a widening of the data points when plotted. Furthermore, implementing a wider range of test parameters in a sequential and iterative manner created much more uniform and consistent results.

A number of wave probes were used in the experiments. It was initially thought that it would be a good idea to have a far field probe, a probe coincident with the impact on the model, and one directly in front of the model to measure reflections. However, the single probe that is coincident with the wave impact on the model provides the most relevant measurements correlated with the spray generation. This was the configuration used in the final tests, which showed good results, and is therefore recommended in further tests.

Taking these two suggestions and combining them with an improved test plan would provide best quality results. The early tests were exploratory in nature as a starting point. The iterative and deliberate test plan created with Design Expert software resulted in the best results. In addition, it is recommended to investigate a higher range of parameters. The wave heights were highest with a wave board frequency setting of 0.8 Hz, so continuing to lower frequencies (with varying spans) would be beneficial.

More interesting imaging results could be obtained by introducing a second camera and using stereo imaging techniques, which serve to resolve spacial depth of view. More accurate estimates of the liquid water content of the spray cloud could then be made.

One of the most natural progressions for this project would be to develop and introduce more realistic hull model shapes. Creating and using strong enough scale vessel hulls, similar to Chung et al. (1998), would facilitate better results. The generated waves could also be created in a more realistic way. Waves containing realistic open sea wave spectra could be used against the newer models. Two more factors could be included to aid in the overall modelling. First, a model velocity in the tow tank could

be introduced to simulate the forward movement of a vessel. Another factor to include could be a wind velocity component that would affect the spray droplet trajectories.

Finally, the ultimate goal of predictive modelling could be worked towards by combining several different approaches. The first approach would be to refine the current work in making correlations between wave characteristics and impact pressure for a given model, along with acquired high speed imaging of the spray fields. The next big development would be to do something similar to Chung et al. (1998), but instead of using cylindrical spray flux collectors, the high speed imaging would be used to perform image analysis, giving an estimate for a spray liquid water content. Equations correlating the wave characteristics to estimated liquid water content could then be used in conjunction with the impact pressure correlations for a more complete modelling tool.

References

Achenbach, E. (1977). The effect of surface roughness on the heat transfer from a circular cylinder to the cross flow of air. *International Journal of Heat and Mass Transfer*, 20:359–369.

Beard, K. and Pruppacher, H. (1969). A determination of the terminal velocity and drag of small water drops by means of a wind tunnel. *Journal of Atmoshperic Sciences*, 26:1066–1072.

Bhattacharyya, R. (1978). *Dynamics of Marine Vehicles*. Ocean Engineering (John Wiley & Sons. Wiley, New York.

Borisenkov, Y. and Pchelko, I. (1975). Indicators for forecasting ship icing. Technical report, United States Army Cold Regions Research Engineering Laboratory, Draft Translation No. 481, Hanover.

Brown, R. and Horjen, I. (1989). Evaluation of state-of-the-art drilling platform icing models. Technical report, Atmospheric Environment Services, Canada, Report No. 89-10.

Brown, R. and Roebber, P. (1985). The scope of the ice accretion problem in canadian waters related to offshore energy and transportation. Technical report, Canadian Climate Centre Report 85-13.

Chung, K. and Lozowski, E. (1998). A three-dimensional time-dependent icing model for a stern trawler. *Journal of Ship Research*, 42(4):266–273.

Chung, K., Lozowski, E., Zakrzewski, W., Gagnon, R., and Thompson, T. (1998). Spraying experiments with a model stern trawler. *Journal of Ship Research*, 42(4):260–265.

Finstad, K., Lozowski, E., and Makkonen, L. (1988). On the median volume diameter approximation for droplet collision efficiency. *Journal of Atmospheric Sciences*, 45(24):4008–4012.

Finstad, K. J. and Lozowski, E. P. (1988). A computational investigation of water droplet trajectories. *Journal of Atmospheric and Ocean Technology*, 5:160–170.

Fisher, R. A. (1966). *The Design of Experiments*. Hafner Publishing Company.

Forest, T., Lozowski, E., and Gagnon, R. (2005). Estimating marine icing on offshore structures using rigice04. International Workshop on Atmospheric Icing of Structures.

Fullerton, A., Fu, T., and Brewton, S. (2010). A comparison of measured and predicted wave-impact pressures from breaking and non-breaking waves. In *28th Symposium on Naval Hydrodynamics*, Pasadena, California.

Glauert, H. (1946). *The elements of aerofoil and airscrew theory*. Cambridge University Press, 2nd edition.

Greco, M., Bouscasse, B., and Lugni, C. (2012). 3-d seakeeping analysis with water on deck and slamming. part 2: Experiments and physical investigation. *Journal of Fluids and Structures*, 33:148–179.

Hay, R. (1956). Ice accumulation upon trawlers in northern waters. *London, Met. Mag*, 85:225–229.

Horjen, I. and Vefsnmo, S. (1984). Mobile platform stability (mops) subproject 02 - icing. mops report no. 15. Technical report, Norwegian Hydrodnamic Laboratories, STF60 A 284002.

Horjen, I., Vefsnmo, S., and Bjerke, P. (1988). Sea spray icing on rigs and supply vessels. Technical report, ESARC.

Itagaki, K. (1977). Icing on ships and stationary structures under marine conditions: A preliminary literature survey of japanese sources. Technical Report 77-27, Cold Regions Research and Engineering Laboratory.

Jones, K. and Andreas, E. (2011). Sea spray concentrations and the icing of fixed offshore structures. *Q. J. R. Meteorol. Soc.*, 138:131–144. DOI:10.1002/qj.897.

Kachurin, L., Gashin, L., and Smirnov, I. (1974). Icing rate of small displacement fishing boats under various hydrometeorological conditions. *Meteorologiya i Gidrologiya, Moscow*, (3):50–60.

Kim, J. and Simon, T. (1993). Journal of heat transfer policy on reporting uncertainties in experimental measurements and results. *Journal of Heat Transfer*, 115:5–6.

Kline, S. J. and McClintock, F. (1953). Describing uncertainties in single sample experiments. *Mech. Eng.*, pages 3–8.

Kultashev, E., Malakhov, N., Panov, V., and Schmidt, M. (1972). Spray icing of srt and srtm fishing vessels. Technical report, United States Army Cold Regions Research Engineering Laboratory, Draft Translation No. 411, Hanover.

Kulyakhtin, A. and Tsarau, A. (2014). A time-dependent model of marine icing with application of computational fluid dynamics. *Cold Regions Science and Technology*,

104-105:33–44.

Lamb, H. (1932). *Hydrodynamics*. Cambridge University Press, sixth edition.

Langmuir, I. and Blodgett, K. (1946). A mathematical investigation of water droplet trajectories. Technical Report 5418, Army Air Forces.

Lebiednzinksi, K. and Thomas, W. (1993). Prediction of bow spray frequency for a naval combatant. In *Proceedings of the 12th International Conference on Port and Ocean Engineering under Arctic Conditions, (POAC), Hamburg*, volume 2, pages 824–834.

Lozowski, E., Stallabrass, J., and Hearty, P. (1983a). The icing of an unheated, nonrotating cylinder. part i: A simulation model. *Journal of Climate and Applied Meteorology*, pages 2053–2062.

Lozowski, E., Stallabrass, J., and Hearty, P. (1983b). The icing of an unheated, nonrotating cylinder. part ii: Icing wind tunnel experiments. *Journal of Climate and Applied Meteorology*, pages 2063–2074.

Lozowski, E., Szilder, K., and Makkonen, L. (2000). Computer simulation of marine ice accretion. *Phil. Trans. R. Soc. Lond. A*, 358:2811–2845.

Makkonen, L. (1985). Heat transfer and icing of a rough cylinder. *Cold Regions Science and Technology*, pages 105–116.

Makkonen, L. and Stallabrass, J. (1987). Experiments on the cloud droplet collision efficiency of cylinders. *Journal of Climate and Applied Meteorology*, pages 1406–1411.

MATLAB (2016). Signal smoothing. `http://www.mathworks.com/help/signal/`

examples/signal-smoothing.html.

Mertins, H. (1968). Icing on fishing vessels due to spray. *Lon. Mar. Obsr.*, 38(221):128–130.

Minsk, D. (1984). Assessment of ice accretion on offshore structures. Technical report, CRREL. Special Report 84-4.

Moffat, R. (1988). Describing uncertainties in experimental results. *Experimental Thermal and Fluid Science*, (1):3–17.

Montgomery, D. C. (1997). *Design and Analysis of Experiments*. John Wiley and Sons.

Muzik, I. and Kirby, A. (1992). Spray overtopping rates for tarsuit island: Model and field study results. *Canadian Journal of Civil Engineering*, 19:469–477.

National Instruments (2016). How to eliminate ac noise when measuring dc signals. http://digital.ni.com/public.nsf/allkb/552D26DA22F4363686257292004O9E6E.

Nature (1881). A singular case of shipwreck. *Nature*, 24(106).

NOAA (2016). Individual vessel icing forecasts for global and regional areas. http://polar.ncep.noaa.gov/marine.meteorology/vessel.icing/. Accessed: 23 February 2016.

Overland, J., Pease, C., and Preisendorfer, R. (1986). Prediction of vessel icing. *Journal of Climate and Applied Meteorology*, 25(12):1793–1806.

Roebber, P. and Mitten, P. (1987). Modelling and measurement of icing in canadian

waters. Technical report, Atmospheric Environment Services, Canada.

Ryerson, C. (1995). Superstructure spray and ice accretion on a large u.s. coast guard cutter. *Atmospheric Research*, 36:321–337.

Ryerson, C. (2013). Icing management for coast guard assets. Technical Report TR-13-7, ERDC/CRREL.

Sawada, T. (1962). Icing on ships and its forecasting. *Japanese Society of Snow and Ice*, 24:12–14.

Stallabrass, J. (1980). Trawler icing: A compilation of work done at n.r.c. Technical Report 19372, National Research Council of Canada, Ottawa, Canada.

Sutherby, F. (1951). Icing problems on ships. *London, J. Glaciol.*, pages 546–548.

Tabata, T. (1969). Studies of ice accumulation on ships, iii. *Low Temperature Science*, Ser. A(27):337–349.

Tabata, T., Iwata, S., and Ono, N. (1963). Studies of ice accumulation on ships, i. *Low Temperature Science*, Ser. A(21):173–221.

Timco, G. and Kubat, I. (2005). Nrc marine icing database. In *Proceedings 11th International Workshop on Atmospheric Icing of Structures (IWAIS), XI.*

Wise, J. and Cominksy, A. (1980). Superstructure icing in alaskan waters, seattle. Technical report, NOAA Special Report, P.M.E.L.

Wu, J. (1979). Oceanic whitecaps and sea state. *Journal of Physical Oceanography*, 9:1064–1068.

Yoon, B. and Ettema, R. (1993). Droplet trajectories and icing-collision efficiencies for cylinders determined using ldv. *Cold Regions Science and Technology*, 21(4):381–397.

Zakrzewski, P. W. (1987). Splashing a ship with collision-generated spray. *Cold Regions Science and Technology*, 14:65–83.

Zakrzewski, P. W. and Lozowski, E. (1988). Estimating the extent of the spraying zone on a sea-going ship. *Ocean Engineering*, 15:413–429.

Zakrzewski, W. (1986). Icing of ships. part i: Splashing a ship with spray. NOAA Tech. Memo., ERL PMEL-66, Pacific Marine Environmental Laboratory, Seattle, WA.

Zarlin, J. (1980). Heat and mass transfer from freely falling drops at low temperature. Technical report, US Army Cold Regions Research and Engineering Laboratory, CRREL Report 80-18.

Appendix A

Tabulated Experimental Results

Tabulated results for each configuration are located within this Appendix. The parameters that were measured and tabulated are the wave height (H_i), wave period (T_i), wavelength ($L_{w,i}$), and impact pressures (P_i). The subscript i denotes which sensor or probe the measurement was taken from. Each value represents the mean of the repeated trials (2-3) for each wave board frequency and span combination used.

Table A.1: Flat Plate Data (Side Position, Spray Perspective)

Frequency (Hz)	Span (%)	H_1 (mm)	H_2 (mm)	H_3 (mm)	T_1 (m)	T_2 (m)	T_3 (m)	$L_{w,1}$ (m)	$L_{w,2}$ (m)	$L_{w,3}$ (m)
1.00	35	198	231	238	1.033	1.017	1.044	1.668	1.613	1.701
0.95	40	218	242	283	1.102	1.071	1.040	1.895	1.791	1.690
1.00	40	221	227	268	1.072	1.065	1.005	1.795	1.771	1.577
0.85	45	358	268	354	1.217	1.147	1.147	2.311	2.053	2.054
0.95	45	211	254	259	1.064	1.041	1.007	1.767	1.691	1.582
0.85	50	332	322	341	1.137	1.170	1.231	2.017	2.137	2.366
0.95	50	176	249	264	1.043	1.068	1.070	1.699	1.780	1.788

Frequency (Hz)	Span (%)	k_1	k_2	k_3	P_A (kPa)	P_B (kPa)	P_C (kPa)	P_D (kPa)	P_E (kPa)
1.00	35	0.119	0.143	0.140	0.285	0.841	0.835	0.970	0.451
0.95	40	0.115	0.135	0.167	0.449	0.883	0.501	0.796	0.586
1.00	40	0.123	0.128	0.170	0.586	0.947	0.702	0.732	0.501
0.85	45	0.155	0.130	0.172	0.713	0.877	0.896	1.093	0.676
0.95	45	0.119	0.150	0.164	0.173	1.210	1.129	1.105	0.618
0.85	50	0.165	0.151	0.144	1.411	1.066	1.124	1.258	0.898
0.95	50	0.104	0.140	0.147	1.548	1.360	1.983	0.484	1.545

Table A.2: Flat Plate Data (Front Position, Sheet Perspective)

Frequency (Hz)	Span (%)	H_1 (mm)	H_2 (mm)	H_3 (mm)	T_1 (m)	T_2 (m)	T_3 (m)	$L_{w,1}$ (m)	$L_{w,2}$ (m)	$L_{w,3}$ (m)
1	35	215	217	211	1.037	1.030	1.070	1.678	1.658	1.788
0.95	40	304	230	279	1.054	1.045	1.047	1.734	1.704	1.711
1	40	207	244	212	1.055	1.025	1.061	1.738	1.640	1.758
0.85	45	272	238	329	1.180	1.170	1.130	2.174	2.137	1.994
0.95	45	281	244	228	1.034	1.027	1.047	1.668	1.646	1.712
0.85	50	275	291	350	1.127	1.087	1.140	1.984	1.844	2.029
0.95	50	259	272	219	1.059	1.031	1.067	1.750	1.659	1.778

Frequency (Hz)	Span (%)	k_1	k_2	k_3	P_A (kPa)	P_B (kPa)	P_C (kPa)	P_D (kPa)	P_E (kPa)
1	35	0.128	0.131	0.118	0.367	0.377	0.642	0.904	0.121
0.95	40	0.175	0.135	0.163	0.503	1.593	1.389	0.761	0.442
1	40	0.119	0.149	0.120	0.261	0.508	0.597	0.562	0.228
0.85	45	0.125	0.111	0.165	1.351	1.002	1.121	1.028	0.793
0.95	45	0.168	0.148	0.133	0.573	1.190	0.958	0.933	0.726
0.85	50	0.139	0.158	0.172	1.653	1.298	1.337	1.029	1.561
0.95	50	0.148	0.164	0.123	1.139	0.748	1.017	1.156	0.465

Table A.3: Flat Plate Data (Front Position, Spray Perspective)

Frequency (Hz)	Span (%)	H_1 (mm)	H_2 (mm)	H_3 (mm)	T_1 (m)	T_2 (m)	T_3 (m)	$L_{w,1}$ (m)	$L_{w,2}$ (m)	$L_{w,3}$ (m)
0.85	50	275	296	419	1.195	1.140	1.220	2.229	2.029	2.324
0.95	50	306	273	333	1.080	1.071	1.110	1.821	1.791	1.925

Frequency (Hz)	Span (%)	k_1	k_2	k_3	P_A (kPa)	P_B (kPa)	P_C (kPa)	P_D (kPa)	P_E (kPa)
0.85	50	0.123	0.146	0.180	0.672	0.973	1.064	1.072	0.978
0.95	50	0.168	0.152	0.173	0.979	1.318	1.817	1.592	0.972

Table A.4: 120^o Model Data (Front Position, Sheet Perspective)

Frequency (Hz)	Span (%)	H_1 (mm)	H_2 (mm)	H_3 (mm)	T_1 (m)	T_2 (m)	T_3 (m)	$L_{w,1}$ (m)	$L_{w,2}$ (m)	$L_{w,3}$ (m)	k_1	k_2	k_3
1	35	193	220	248	0.950	0.999	0.980	1.409	1.558	1.501	0.137	0.141	0.165
0.95	40	203	199	249	0.983	1.018	1.070	1.508	1.617	1.788	0.135	0.123	0.139
1	40	202	226	247	0.917	1.017	0.972	1.313	1.614	1.475	0.154	0.140	0.167
0.85	45	255	235	261	1.197	1.254	1.223	2.236	2.455	2.336	0.114	0.096	0.112
0.95	45	194	208	241	0.962	1.090	0.985	1.446	1.857	1.514	0.134	0.112	0.159
0.85	50	266	239		1.200	1.145	0.000	2.250	2.046		0.118	0.117	
0.95	50	190	230	232	1.004	1.045	1.110	1.573	1.705	1.923	0.120	0.135	0.121
0.85	55	255	240	251	1.177	1.213	1.202	2.165	2.298	2.255	0.118	0.104	0.111

Table A.5: 120^o Model Data (Front Position, Spray Perspective)

Frequency (Hz)	Span (%)	H_1 (mm)	H_2 (mm)	H_3 (mm)	T_1 (m)	T_2 (m)	T_3 (m)	$L_{w,1}$ (m)	$L_{w,2}$ (m)	$L_{w,3}$ (m)	k_1	k_2	k_3
1	35	199	199	204	0.990	0.984	0.994	1.531	1.512	1.543	0.130	0.132	0.132
1	40	200	226	187	0.963	1.008	0.992	1.449	1.586	1.536	0.138	0.143	0.122
0.85	45												
0.95	45	170	202	212	1.065	1.045	1.035	1.771	1.704	1.672	0.096	0.118	0.126
0.85	50	246	246	264	1.146	1.163	1.197	2.052	2.113	2.238	0.120	0.116	0.118
0.95	50	192	201	248	1.020	1.031	1.056	1.624	1.660	1.742	0.118	0.121	0.142
0.75	55	270	255	289	1.385	1.321	1.290	2.995	2.725	2.599	0.090	0.094	0.111
0.8	55	236	224	266	1.190	1.206	1.235	2.211	2.271	2.380	0.107	0.099	0.112
0.85	55	245	227	281	1.204	1.171	1.107	2.262	2.140	1.913	0.108	0.106	0.147
0.9	55	216	206	226	0.977	1.094	1.146	1.490	1.869	2.049	0.145	0.110	0.110

Table A.6: 120^o Model Data (Side Position, Sheet Perspective)

Frequency (Hz)	Span (%)	H_1 (mm)	H_2 (mm)	H_3 (mm)	T_1 (m)	T_2 (m)	T_3 (m)	$L_{w,1}$ (m)	$L_{w,2}$ (m)	$L_{w,3}$ (m)	k_1	k_2	k_3
1	35	195	201	193	1.017	0.990	0.970	1.615	1.530	1.469	0.121	0.131	0.131
1	40	183	176	212	0.944	0.940	0.907	1.390	1.380	1.285	0.131	0.127	0.165
0.85	45	225	215	240	1.195	1.115	1.125	2.229	1.941	1.975	0.101	0.111	0.121
0.85	50	219	221	250	1.174	1.165	1.250	2.153	2.120	2.439	0.102	0.104	0.102
0.8	55	252	228	254	1.191	1.217	1.173	2.216	2.314	2.150	0.114	0.099	0.118
0.85	55	252	199	259	1.134	1.180	1.128	2.007	2.173	1.988	0.125	0.091	0.130
0.9	55	218	178	268	1.069	1.084	1.083	1.785	1.834	1.832	0.122	0.097	0.146

Table A.7: 135° Angle Data (Side Position)

Frequency (Hz)	Span (%)	H_1 (mm)	H_2 (mm)	T_1 (s)	T_2 (s)	$L_{w,1}$ (m)	$L_{w,2}$ (m)	k_1	k_2	P_A (kPa)	P_B (kPa)	P_C (kPa)
0.80	35	283	339	1.260	1.250	2.440	2.479	0.116	0.137	1.498	0.489	1.019
0.80	40	286	350	1.220	1.260	2.479	2.324	0.115	0.150	1.516	0.856	1.217
0.80	45	271	273	1.135	1.240	2.401	2.011	0.113	0.135	1.696	0.510	1.043
0.80	50	330	266	1.110	1.150	2.065	1.924	0.160	0.138	1.602	0.316	0.934
0.80	55	266	288	1.150	1.255	2.459	2.065	0.108	0.139	1.603	0.240	0.945
0.85	35	271	243	1.160	1.230	2.362	2.101	0.115	0.116	1.603	0.517	1.015
0.85	40	251	260	1.110	1.185	2.192	1.924	0.114	0.135	1.496	0.314	0.920
0.85	45	245	248	1.115	1.165	2.119	1.941	0.115	0.128	1.463	0.362	0.948
0.85	50	238	248	1.180	1.115	1.941	2.174	0.122	0.114	1.446	0.325	0.894
0.85	55	230	238	1.095	1.140	2.029	1.872	0.113	0.127	1.419	0.207	0.753
0.90	35	245	225	1.090	1.120	1.959	1.855	0.125	0.121	1.534	0.378	0.985
0.90	40	235	212	1.080	1.130	1.994	1.821	0.118	0.116	1.361	0.101	0.715
0.90	45	233	226	1.070	1.135	2.011	1.788	0.116	0.126	1.393	0.211	0.958
0.90	50	223	205	1.020	1.130	1.994	1.624	0.112	0.126	1.511	0.354	1.102
0.90	55	200	206	1.000	1.080	1.821	1.561	0.110	0.132	1.393	0.331	0.874
0.95	35	228	198	1.060	1.065	1.771	1.754	0.129	0.113	1.393	0.276	0.798
0.95	40	213	158	1.020	1.045	1.705	1.624	0.125	0.097	1.226	0.164	0.616
0.95	45	216	186	1.005	1.095	1.872	1.577	0.115	0.118	1.168	0.155	0.591
0.95	50	178	187	1.035	1.020	1.624	1.673	0.110	0.112	1.155	0.112	0.745
0.95	55	182	217	1.115	1.085	1.838	1.941	0.099	0.112	1.103	0.173	0.609
1.00	35	177	159	0.980	0.940	1.380	1.500	0.128	0.106	1.079	0.118	0.533
1.00	40	167	155	1.000	0.980	1.500	1.561	0.111	0.099	1.244	0.148	1.334

Table A.8: 135° Model Data (Side Position, $\alpha = 20°$)

Frequency (Hz)	Span (%)	H_1 (mm)	H_2 (mm)	T_1 (s)	T_2 (s)	$L_{w,1}$ (m)	$L_{w,2}$ (m)	k_1	k_2	P_A (kPa)	P_B (kPa)	P_C (kPa)
0.80	35	272	261	1.205	1.230	2.362	2.267	0.115	0.115	2.049	0.824	1.821
0.80	40	303	320	1.255	1.305	2.659	2.459	0.114	0.130	1.619	0.696	1.154
0.80	45	272	274	1.100	1.185	2.192	1.889	0.124	0.145	1.726	2.846	1.563
0.80	50	280	323	1.215	1.250	2.440	2.305	0.115	0.140	1.543	1.325	1.159
0.80	55	267	318	1.230	1.240	2.401	2.362	0.111	0.134	1.121	0.556	1.151
0.85	35	275	269	1.135	1.160	2.101	2.011	0.131	0.133	1.402	0.523	0.888
0.85	40	255	229	1.145	1.170	2.137	2.047	0.119	0.112	1.721	0.487	0.969
0.85	45	252	244	1.085	1.165	2.119	1.838	0.119	0.132	1.476	0.431	1.433
0.85	50	230	223	1.120	1.170	2.137	1.959	0.107	0.114	1.468	0.253	0.810
0.85	55	241	200	1.120	1.145	2.047	1.959	0.117	0.102	1.507	0.436	2.054
0.90	35	232	190	1.030	1.100	1.889	1.656	0.123	0.115	1.328	0.260	0.953
0.90	40	277	205	1.115	1.115	1.941	1.941	0.143	0.106	1.316	0.217	1.151
0.90	45	221	197	1.100	1.095	1.872	1.889	0.118	0.104	1.225	0.209	0.670
0.90	50	228	205	0.965	1.055	1.738	1.454	0.131	0.141	1.356	0.345	1.142
0.90	55	185	167	1.025	1.065	1.771	1.640	0.104	0.101	1.430	0.468	1.390
0.95	35	226	184	1.020	1.060	1.754	1.624	0.129	0.113	1.213	0.161	0.982
0.95	40	201	184	0.990	1.040	1.689	1.530	0.118	0.113			
0.95	45	206	180	1.050	1.055	1.738	1.721	0.119	0.120	1.270	0.140	0.805
0.95	50	170	160	1.030	0.955	1.424	1.656	0.119	0.096	1.537	0.200	0.962
0.95	55	166	175	0.990	1.030	1.656	1.530	0.100	0.114	0.998	0.110	0.512
1.00	35	181	168	0.915	1.045	1.705	1.307	0.106	0.129	1.805	0.122	1.227
1.00	40	162	157	0.990	1.000	1.561	1.530	0.103	0.102	1.085	0.125	0.439

Table A.9: 135° Model Data (Front Position, $\alpha = 20°$)

Frequency (Hz)	Span (%)	H_1 (mm)	H_2 (mm)	T_1 (s)	T_2 (s)	$L_{w,1}$ (m)	$L_{w,2}$ (m)	k_1	k_2	P_A (kPa)	P_B (kPa)	P_C (kPa)
0.80	45	298	315	1.040	1.250	2.440	1.689	0.122	0.186	1.584	0.735	1.109
0.80	50	302	268	1.215	1.230	2.362	2.305	0.128	0.116	1.606	0.562	1.037
0.80	55	273	276	1.155	1.250	2.440	2.083	0.112	0.132	1.121	0.555	1.151
0.85	35	273	247	1.000	1.170	2.137	1.561	0.128	0.158	1.708	0.633	1.364
0.85	50	244	172	1.210	1.115	1.941	2.286	0.126	0.075	1.059	0.139	0.618
0.85	55	243	230	1.110	1.170	2.137	1.924	0.114	0.119	1.353	0.236	1.038
0.90	35	236	209	1.095	1.030	1.656	1.872	0.142	0.112	1.600	0.338	1.193
0.90	55	198	187	1.050	1.030	1.656	1.721	0.119	0.108	1.476	0.366	1.338
0.95	45	206	181	1.045	0.960	1.439	1.705	0.143	0.106	1.395	0.180	1.074